Montanuniversität Leoben

Hard coatings with designed anisotropic thermal conductivity

Diploma Thesis
by
Katharina Skalnik
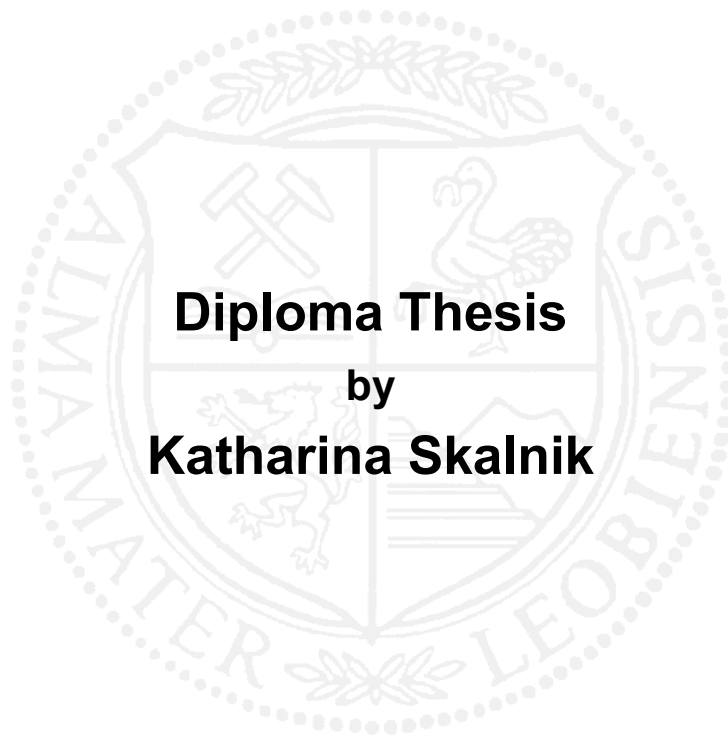
This work has been carried out with at the Materials Center Leoben and the Chair of Functional Materials and Materials Systems at the Department of Physical Metallurgy and Materials Testing, Montanuniversität Leoben, Austria.

Leoben, August 2017

Affidavit:

I declare in lieu of ought, that I wrote this thesis and performed the associated research myself, using only literature cited in this work.

Leoben, August 2017

Acknowledgments

My sincerest gratitude is due to Univ.-Prof. DI Dr. Christian Mitterer for providing me with the opportunity to carry out this work at the Chair of Functional Materials and Materials Systems.

A huge thank you goes to Michael for his patience and great support while supervising me at writing this thesis. He always answered my questions and helped me whenever it was necessary.

I would also like to express my gratitude to all members of the thin film group for the great support and the pleasurable working atmosphere. Especially, I am grateful to Veli and Rosti for helping me a lot carrying out the deposition runs of this work.

Furthermore, I would like to thank Dr.rer.nat. Markus Winkler of the Fraunhofer Institute of Physical Measurement Techniques for carrying out the TDTR measurements.

A special thanks goes to all my friends that came into my live in Leoben for always being there for me in good and hard times.

The biggest thanks goes to my family for their great support and love they are giving me.

Table of Contents

1 Introduction

Due to their high hardness and chemical stability, hard coatings are often used to protect tools for cutting applications. In particular, $Ti_{1-x}Al_xN$ based coatings are frequently applied because of their favorable properties at elevated temperatures, such as oxidation resistance and high temperature hardness. Optimizing specific properties to increase the performance of such coatings has been subject of investigations for more than two decades. Nevertheless, the thermal conductivity has only been an additional invasion, but recently gains increasing interest in research [1,2].

$Ti_{1-x}Al_xN$ represents a metastable solid solution and tends to decompose into cubic (c)-TiN and c-AlN at elevated temperatures. Simultaneously, phase transformation of the formed c-AlN into wurtzitic (w)-AlN takes place. With on-going spinodal decomposition and subsequent phase transformation, an increasing thermal conductivity was reported [3]. The observed values exceed the initial thermal conductivity to a great extent. However, fundamental design rules for the thermal conductivity of wear resistant coatings are missing; thus, a correlation of conductivity with cutting performance is not possible. Nevertheless, several concepts have been suggested to improve the thermal management during cutting. One of these concepts is to use coatings with anisotropic thermal conductivity as proposed by Böttger et al. [1,4,5]. For example, the proposed anisotropy can be established with multilayer structures consisting of two alternating layers with high and low thermal conductivities. The result is that the thermal conductivity parallel to the surface (in-plane) is higher than perpendicular to the surface (cross-plane). Böttger et al. showed that a pronounced anisotropy can reduce thermal gradients on interfaces between coating and substrate. Subsequently, they created a model to calculate the anisotropy of the thermal conductivity from the individual thermal conductivities of alternating layers [4,5].

Consequently, this work concentrates on synthesis and characterization of coatings with significant anisotropy in thermal conductivity. Alternating multilayers of SiO_x and $Ti_{1-x}Al_xN$ were deposited in order to obtain a difference of in- and cross-plane thermal conductivity. Additionally, the thermal conductivity of selected $Ti_{1-x}Al_xN$ samples was altered, utilizing post deposition annealing, to gain an increase in anisotropy. The thermal conductivity of the synthesized coatings was determined by time-domain thermoreflectance (TDTR). Cross-plane measurements were performed on the sample surfaces. For in-plane measurements, cross-sections of the samples were generated using ion-beam assisted sample preparation. Thus, an anisotropy factor of

the tested samples could be calculated from the obtained in- and cross-plane thermal conductivities.

The present work aims towards the development of a comprehensive methodology to investigate anisotropic thermal conductivities. Special emphasis was laid on the preparation of cross-sectional samples and the measurement of the in-plane thermal conductivity. This work significantly contributes towards utilization of tailored thermal conductivities of hard coatings as a further playground to optimize coating performance.

2 Theoretical Background

2.1 Physical Vapor Deposition

Different physical vapor deposition (PVD) techniques are available, e.g. electron-beam evaporation, arc evaporation or sputtering [6]. For all of these techniques, a condensable vapor of molecules or atoms is created from a solid or liquid target material and is transported to the substrate in a vacuum or low pressure gaseous environment [7]. Not only is the substrate coated, but also the whole vacuum chamber in line-of-sight to the target. To obtain a homogeneous coating, sophisticated substrate rotation is necessary [8,9].

PVD methods, especially sputtering, are suitable to deposit multicomponent coatings with different elements [10]. To synthesize compounds, reactive processes are often utilized, where a reactive gas, for example O_2 or N_2, is inserted into the vacuum chamber to create the aimed for nitride or oxide [6]. The coatings for this work were synthesized by sputter deposition, which will be briefly described in section 2.1.1.

2.1.1 Sputter Deposition

The PVD process with the most widespread use is sputter deposition. There, the vacuum chamber is filled with a working gas, often Ar. Between the target, forming the cathode, and the substrate or the chamber walls, forming the anode, a plasma is ignited. Here, highly energetic ions are generated and bombard the target to physically evaporate atoms. After this creation of a vapor phase, the atoms which move towards the substrate form the coating [6,7].

Sputtering can be done in different modes, which are direct-current (DC), pulsed DC and radio-frequency (RF). DC sputtering is an often used method because of cheap power supplies and easy process control. For RF sputtering, the discharges operate in the MHz frequency range and for the pulsed DC mode in the kHz frequency range, where the applied voltage can be pulsed bipolarly or unipolarly [6].

For DC sputter deposition, the power supply is a high-voltage DC source. The target serves as the cathode of the discharge and the anode can be the substrate and/or the walls of the vacuum chamber. The plasma is created and supported by the DC source via secondary electron emission at the cathode and impact ionization of neutral gas atoms [7].

When a DC potential is applied to grow compound coatings by reactive deposition, the target may become completely covered with a dielectric material with low electrical conductivity. Consequently, the flux of ions or electrons is hindered, the

deposition process is slowed down and arcs can be formed. If pulsed DC or RF sputtering is utilized, charged surfaces are permanently discharged; ions and electrons can continuously move between the electrodes. During the positive pulse, electrons move to the target and neutralize any charge, which was built up during the negative pulse. During this negative pulse, intense energetic sputtering of dielectric target surfaces by positive ions occurs. The optimal frequency of pulsing and the pulse duration together with the relative pulse height strongly depends on the target material [8].

To deposit compounds reactive sputtering is widely used. There, the deposition is done by sputtering from metallic targets in the presence of a reactive gas and a working gas (normally argon). Some typically used reactive gases are nitrogen or oxygen [11].

The potential formed between plasma and substrate surface can be increased by applying an externally generated negative bias potential on the substrate, which attracts positive ions from the plasma to bombard the substrate. The concurrent bombardment increases the mobility of condensed atoms, the surface diffusion and therefore increases the density of the growing film. The bias potential can be formed with continuous DC, pulsed DC, alternating-current (AC) or RF voltages [8].

For magnetron sputtering, permanent magnetic fields are applied to trap the electrons in front of the so-called magnetron covered by the target and consequently also the Ar^+ ions are concentrated near the target surface. Due to the resulting higher electron and ion density, a higher sputtering rate is obtained. Magnetrons can be balanced or unbalanced, depending on the looping of the magnetic field lines. If the magnetron is balanced, the magnetic field lines are self-contained and only loop between the central and the outer magnets. In an unbalanced magnetron, the magnetic field lines also loop between the central and the much stronger outer magnets, but are also open towards the substrate. Thus, the plasma is allowed to expand away from the target area and the electrons are guided towards the substrate surface [6]. A schematic of an unbalanced magnetron sputter system is illustrated In Figure 2-1(a).

Figure 2-1(b) shows that the transformation of the target material into the gaseous phase occurs directly as a result of an atomic momentum transfer [10]. There, the impinging gas ion transfers its impulse to the target atoms and creates a collision cascade. When these collisions move towards the surface, atoms are ejected from the target if they obtain enough kinetic energy [12].
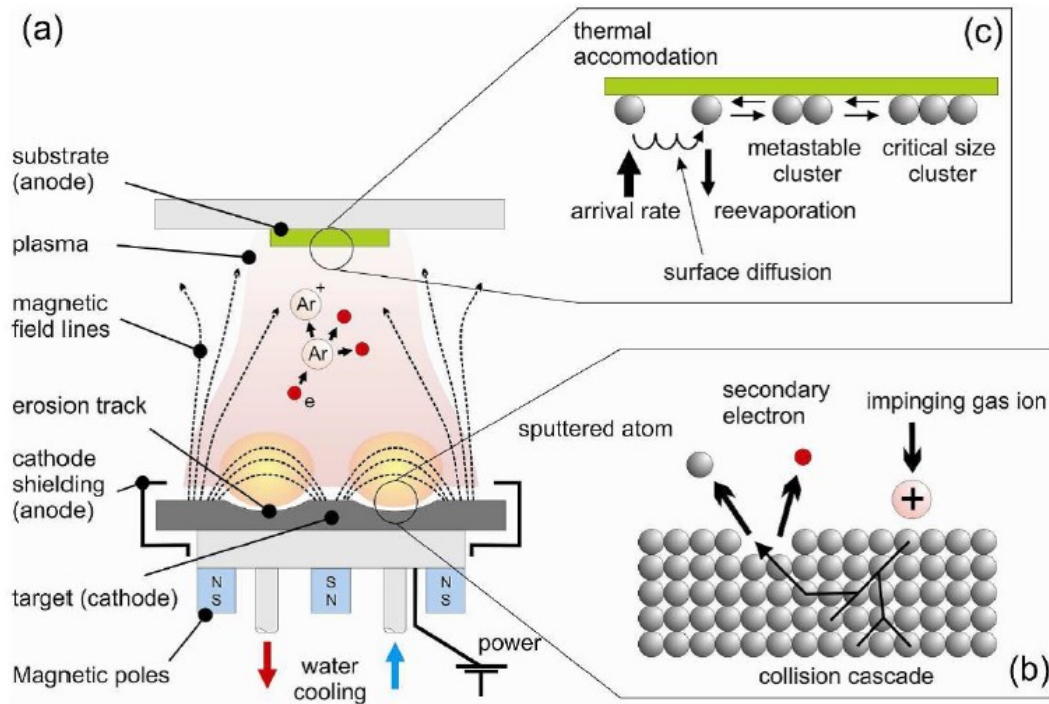
Figure 2-1: (a) Schematic representation of a magnetron sputtering system, which shows the most important processes during (b) the sputter procedure at the target and (c) the nucleation process at the sample surface [13].

The target atoms which are ejected move through the plasma (Figure 2-1(a)) and arrive at the substrate (Figure 2-1(c)). The arriving atoms migrate via surface diffusion and can either re-evaporate or form metastable clusters. If these metastable clusters form stable clusters during nucleation, grain growth can start [12,13].

The microstructure and morphology of the forming coating is influenced by the mobility of the ad-atoms, their diffusion on the surface and eventually also by bulk-diffusion. It also strongly depends on substrate temperature and energetic bombardment by atoms or ions, which transfer their kinetic energy to the film forming species. The structure zone model (SZM) shown in Figure 2-2 is used to describe the formed morphologies [11,12]. Four different structural zones can be described as a function of Ar pressure and the temperature T/T_m, where T is the substrate temperature and T_m the melting temperature of the coating material. In Zone 1 at low substrate temperatures, the observed coatings are porous and consist of crystals with domed tops. This leads to a rough surface as a result of low surface diffusivity. Higher pressures push the borders of Zone 1 to higher substrate temperatures. The ad-atom mobility increases with higher temperatures and more nuclei are formed. This leads to Zone T, which is controlled by competitive growth. At the even higher temperatures in Zone 2, the columnar grains consolidate and coarsen due to increased diffusivity. In Zone 3 at still higher temperatures, equiaxed grains are formed. Thus, the coating surface becomes smoother [14].
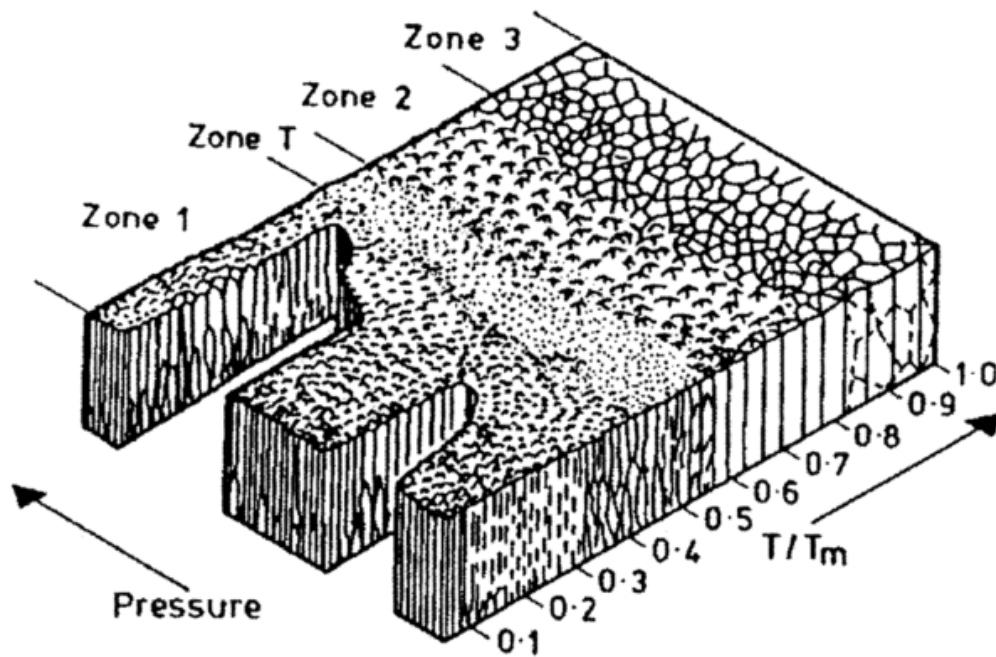
Figure 2-2: Structure zone model by Thornton for magnetron sputtering [14].

The big advantage of sputtering is the obviation of droplet formation (a typical disadvantage of arc evaporation), which results in the formation of films with smooth surfaces. However, the with about 1 % low ionization rate of the sputtered species can be a disadvantage, since the low number of ionized film forming species limits the possibility of accelerating them to the substrate by an applied bias voltage to promote film growth [6].

2.2 Thermal Conductivity

2.2.1 Introduction

The thermal conductivity can be described as the transfer of thermal energy within a material, which is taking place by the movement of free electrons and phonons. Two contributions to thermal conductivity can be distinguished, i.e. the phononical and the electronical thermal conductivity. Metals often have a higher thermal conductivity than non-metals, because of the free electrons, which are responsible for the electrical conductivity and at the same time take part in transport of heat [15–17].

If lattice defects, like interstitials, vacancies or dislocations are present, the scattering of phonons in the crystal structure increases, which consequently reduces the thermal conductivity [5]. The thermal conductivity is inversely proportional to the specific surface of grain boundaries [2].

2.2.2 Thermal Conductivity of Hard Coatings

Hard coatings are widely used for cutting applications, where often high temperature is prevailed [4]. Thus, cutting tools are frequently coated with hard coatings to provide the required high wear resistance. These coatings should have a good chemical stability, oxidation resistance, diffusion resistance, hardness and a good adhesion to the substrate [2].

When searching for optimized coating systems for cutting applications, the thermal conductivity often only has been an additional invasion. More recently, the thermal conductivity moved into the focus of research. There are diverse promising concepts for thermal management for cutting applications [1,2,4,5,18]. The thermal conductivity of hard coatings can be measured by the TDTR method, which will be described in section 2.2.4 [19].

One of these concepts is the use of coatings as a thermal barrier to redirect the heat flow into the chip and thereby protecting the tool and the work piece. Hence, the thermal conductivity of these coatings should be as low as possible, especially at high temperatures [2]. Many of the microstructural features that increase hardness, such as small grain sizes, nano-precipitates and strengthened grain boundaries simultaneously hinder the heat transport and thus lower the thermal conductivity [18].

Another approach is to consider the coating as a heat sink, to protect the tool from local temperature maxima and high temperature gradients. Here a high thermal conductivity is needed [2,18].

The concept, which motivates this work, is based on an anisotropic thermal conductivity within a coating to be used for e.g. wear protection of cutting tools. With this anisotropy, the heat flow can be redirected into the chip and out of the coating/substrate system, resulting in a higher life span [1,5].

Hard coatings often consist of transition metal nitrides, which crystallize in a cubic structure resulting in isotropic thermal properties. It is still possible to induce anisotropy in intrinsically isotropic materials by engineering them at micro- and nanoscale. This can be achieved by specific oriented crystallites, grain boundaries, nanostructures or multilayer systems, where the sub-layers exhibit different thermal conductivities [4].

2.2.3 Anisotropy of Thermal Conductivity in Multilayer Coatings

Multilayer architectures provide the potential to tailor microstructure as well as mechanical and thermal properties of hard coatings. Multilayered coatings with alternating layers of two or more different materials can combine the advantages of the contained layers. Furthermore, the interface between the different sub-layers is

considered as a barrier to dislocation motion, crack propagation and element diffusion, especially when the layer thickness is reduced to nanoscale [20].

A high anisotropy of the thermal conductivity can be achieved with a multilayer structure comprising two alternating layers, one with a high and the other one with a low thermal conductivity. The result is that the thermal conductivity parallel to the surface (in-plane) is higher than perpendicular to the surface (cross-plane). Therefore, in-plane thermal gradients at the tool surface are reduced and the heat flow into the chip and out of the layer/substrate system is enhanced [5]. This design might be effective for processes that involve short contact times and small contact areas such as hobbing and milling [4].

Another way to gain high thermal anisotropy is to combine different material classes such as metals with ceramics or amorphous with crystalline materials. This would also result in high thermal interface resistance between sub-layers. However, due to the differences in thermal expansion, hardness and toughness, it would be difficult to engineer coatings which are appropriate for high thermal and high mechanical load applications [4].

A thermal resistor model has been suggested for the anisotropy of a periodic multilayer structure [1]. There, the thicknesses x of two sub-layers 1 and 2 differ by a factor of $a = x_1/x_2$ and the thermal conductivity κ differs by a factor of $b = \kappa_1/\kappa_2$. If the model is set as independent of the absolute thickness, the in-plane and the cross-plane thermal conductivity are defined by

$$\kappa\| = \frac{\kappa_2(1+ab)}{1+a} \text{ and } \kappa \perp = \kappa_2 \frac{b(1+a)}{a+b}. \tag{1}$$

Now the anisotropy factor F of the thermal conductivity can be calculated with

$$F = \kappa\|/\kappa \perp. \tag{2}$$

The anisotropy factor only depends on the relative thermal conductivity and the thickness of the two layers. This thermal resistor model is applicable to any multilayer system containing periodic alternating layers [1].

2.2.4 Time-Domain Thermoreflectance

For the TDTR method an optical modulation process is used, where the change of the optical constants as a response to an impressed periodic perturbation is measured. This perturbation is, in the case of the TDTR, thermal energy which is submitted by a laser beam, the so called pump beam. The resulting change of the optical constant is detected by a second laser beam, the probe beam [19].

TDTR can be used to determine the thermal conductivity of hard coatings and multilayer structures with the aid of numerical models. This method utilizes the

change in reflectivity of a well-defined sample surface, due to the inducted difference in temperature. For the measurement, the surface of the coatings needs to be mirror polished and coated with a ~70 nm thick layer, typically Al, to obtain a well-defined temperature dependent reflectivity. Thus, a high intensity of the probe beam reflected from the sample surface is provided [4,19]. The required electrical and thermal conductivity of the Al layer are calculated with the van-der-Pauw and the Wiedemann-Franz law, where also its thickness needs to be exactly known [17].

The advantages of the TDTR-method are [19]:

- The possibility to measure thin films on micro- and nanoscale.
- The relatively simple sample preparation.
- A high local resolution.
- The possibility to measure multilayer structures.
- A simple and flexible sample handling.

In Figure 2-3 the measurement setup is schematically shown. First, a pulsed laser beam is generated by a Ti-sapphire laser. Then, the beam passes through two $\lambda/2$ plates and an optical isolator to regulate the polarization and the total power. Subsequently, the beam is separated into the pump beam (vertically polarized) and the probe beam (horizontally polarized) with a polarizing beam splitter. The pump beam is used to heat the sample, whereas the created temperature profile is scanned by the probe beam [19].

Before the beams arrive on the sample, a delay between them has to be generated, by passing the pump beam through a mechanical delay line. This delay line is needed to adjust variable time differences between the pump and probe beam to measure the time dependent evolution of temperature dependent reflectivity of the Al layer. The probe beam meanwhile passes through a mechanical chopper, a non-polarizing laser splitter, a focusing objective and is afterwards directed towards the sample, which is located in an adaptable sample holder. Before the pump beam reaches the sample, it passes another polarizing beam splitter to the same focusing objective as the probe beam [19].

The reflected vertically polarized part of the pump beam should not be seen by the photo detector and is thus nearly completely reflected by a polarized beam splitter beside the sample holder. The reflected probe beam passes the two beam splitters of the pump and the probe beam and is then led to the third non-polarizing beam splitter. There, a part of the beam is guided to the CCD-camera with an up streamed color filter. The CCD-camera is used to observe the sample surface and the beam position. The other part of the beam is directed towards the photo detector [19].
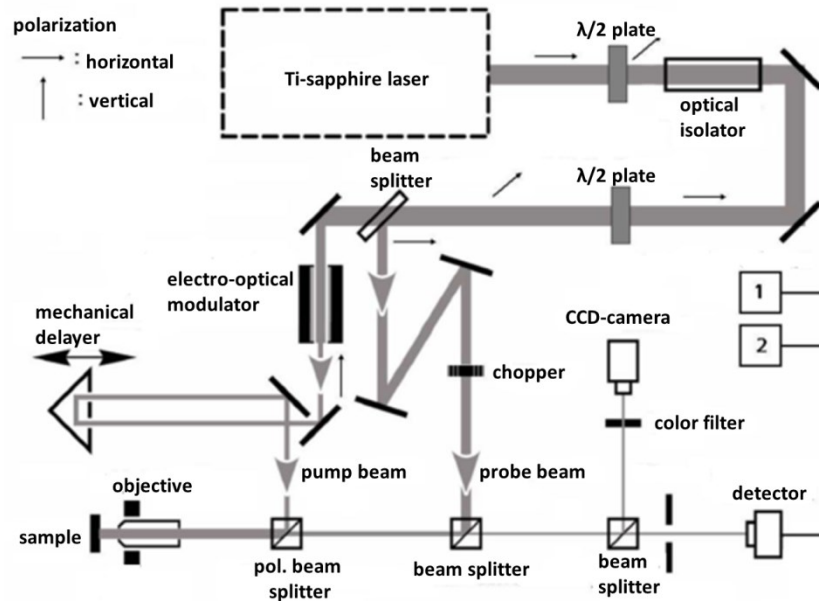
Figure 2-3: Schematics of the measurement setup of a TDTR apparatus with the different paths of pump and probe beam [19].

2.3 The Ti-Al-N System

TiN is a widely used hard coating material. However, major drawbacks are its relatively low hardness and oxidation resistance at elevated temperatures. In contrast, AlN is characterized by an excellent thermal stability and good mechanical properties. The combination of both yields a metastable cubic solid solution of TiN and AlN, leading to $Ti_{1-x}Al_xN$ coatings with improved properties [21,22]. These coatings provide an improved oxidation behavior, due to the formation of a protective Al-rich oxide layer at the film surface, if exposed to high temperatures, high hardness and chemical stability. Therefore, they gained huge importance for industrial applications [23,24].

The $Ti_{1-x}Al_xN$ solid solution can be synthesized by PVD techniques, even though c-TiN and c-AlN exhibit essentially no mutual solubility, tend to decompose and exhibit a wide miscibility gap at low temperatures [25]. To create this metastable c-$Ti_{1-x}Al_xN$ solid solution, deposition conditions far from the thermodynamic equilibrium are needed. $Ti_{1-x}Al_xN$ contains two cubic sub-lattices, where one is fully occupied by nitrogen and the other one is randomly populated by composition dependent Al and Ti atoms [3,26].

For c-$Ti_{1-x}Al_xN$, the hardness, the oxidation resistance and the thermal stability increases with the AlN fraction x, which also has an influence on the microstructure of the deposited coatings [27]. The microstructural evolution versus x is summarized

in Figure 2-4. Up to x = 0.65, Al can be incorporated on the metal sub-lattice within the c-TiN to form the metastable solid solution $c\text{-}Ti_{1-x}Al_xN$. For $0.65 \leq x \leq 0.75$, this is no longer possible and a dual phase structure of $c\text{-}Ti_{1-x}Al_xN$ and a solid solution of $w\text{-}Al_xTi_{1-x}N$ appear. When x is higher than 0.75, a metastable $w\text{-}Al_xTi_{1-x}N$ solid solution is formed [24].
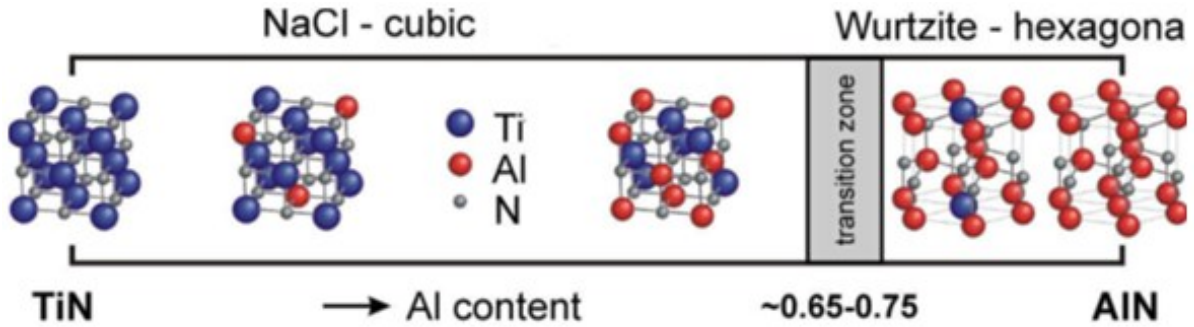

Figure 2-4: Schematics of the microstructural evolution in $Ti_{1-x}Al_xN$ versus AlN content [28].

In Figure 2-5 (a) a possible schematic structure of as deposited $c\text{-}Ti_{1-x}Al_xN$ is shown. Since $c\text{-}Ti_{1-x}Al_xN$ is a metastable solid solution, spinodal decomposition into c-AlN rich and c-TiN rich domains takes place at elevated temperatures of about 900°C [27], as seen in Figure 2-5 (b). While the decomposition is on-going, also phase transformation of the formed metastable c-AlN into the stable w-AlN occurs, which is associated with a volume increase of about 25% [25] (Figure 2-5 (c)). With rising temperature, the Al diffuses out of the c-TiN and grain growth occurs. This is illustrated in Figure 2-5 (d). In Figure 2-5 (e), the coarsening of the resulting dual phase system and the reduction of the number of grain boundaries can be seen [3].
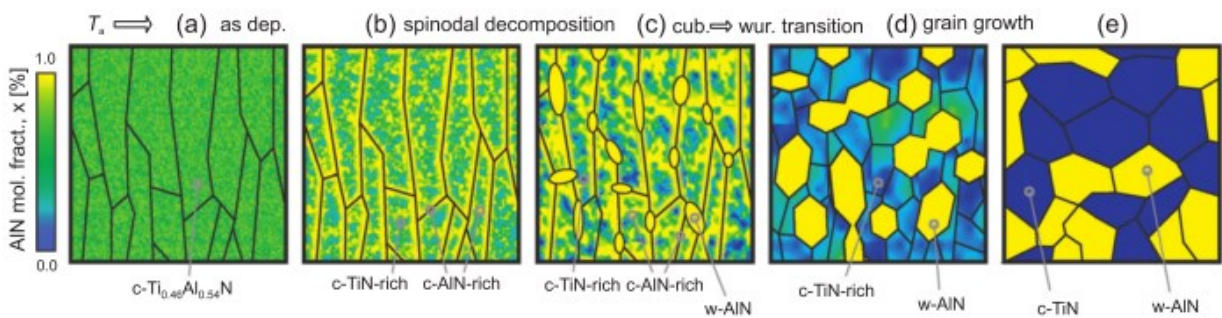

Figure 2-5: Schematic structural evolution of $c\text{-}Ti_{1-x}Al_xN$ during annealing with (a) the as-deposited state, (b) spinodal decomposition into c-AlN-rich and c-TiN-rich domains, (c) phase transformation of c-AlN to w-AlN, (d) diffusion of Al out of c-TiN and grain growth and (e) coarsening of the dual phase structure [3].

Coatings with a large single-phase field, such as TiN, normally soften due to recovery, recrystallization and grain growth at elevated temperatures. In comparison, the metastable $c\text{-}Ti_{1-x}Al_xN$ owns a substantial hardness increase with increasing temperature. The hardness development over annealing temperature for TiN and

$Ti_{1-x}Al_xN$ is visualized in Figure 2-6. The obvious hardness increase is the result of spinodal decomposition. The different lattice parameters of c-TiN and c-AlN cause coherency strains, which foster strain hardening of $Ti_{1-x}Al_xN$ due to the hindered dislocation motion. As soon as c-AlN transforms into w-AlN, the hardness of $Ti_{1-x}Al_xN$ decreases (Figure 2-6). This stems from the coarsening of the grains, the loss of coherency strains between c-TiN and w-AlN and the lower hardness of w-AlN with respect to c-AlN [25,26].
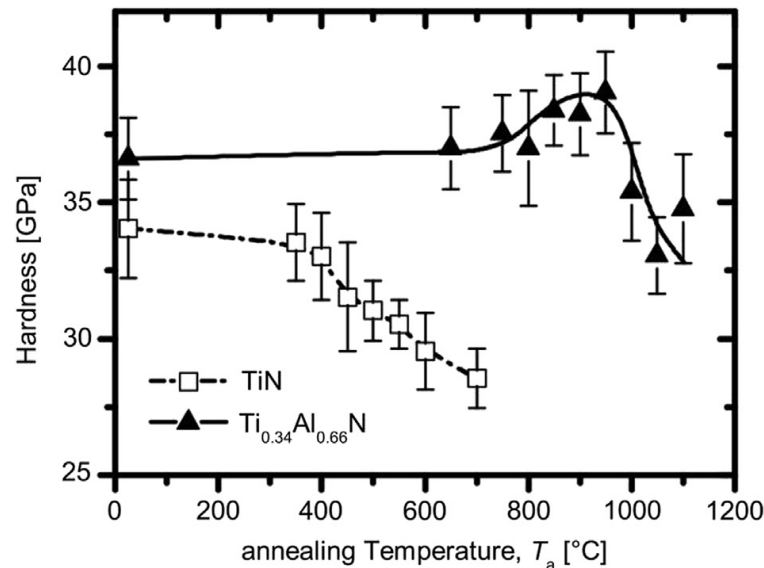

Figure 2-6: Coating hardness versus annealing temperature for TiN and $Ti_{0.34}Al_{0.66}N$ with the low high-temperature hardness of TiN compared to the superior hardness of $Ti_{1-x}Al_xN$ [25].

In Figure 2-7 the thermal conductivity of Ti1-xAlxN versus annealing temperature is shown. First, the thermal conductivity slightly increases due to recovery and formation of c-AlN rich and c-TiN rich domains with enhanced thermal conductivity. With further annealing, the transformation of c-AlN into w-AlN starts and the conductivity decreases again due to the extended phonon scattering at domain interfaces and grain boundaries. At higher temperatures, when c-AlN is completely transformed into w-AlN, the thermal conductivity increases significantly. This is taking place since the reduction of the number of grain boundaries due to coarsening of the dual phase structure reduces phonon scattering. Also, the thermal conductivity of w-AlN is higher than that of c-AlN [3]. The literature values of the single phases, which are formed during annealing of $Ti_{1-x}Al_xN$, are summarized in Table 1 [22,29,30].
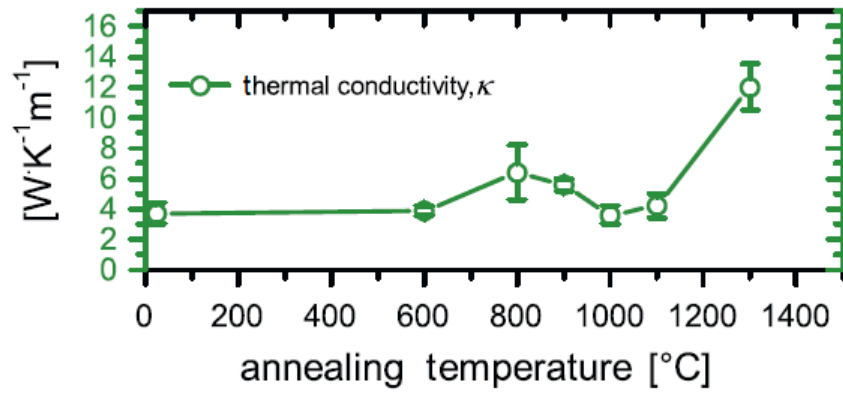
Figure 2-7: Thermal conductivity as a function of the annealing temperature of Ti$_{1-x}$Al$_x$N with increasing thermal conductivity at high temperatures [3].

Table 1: Literature values of thermal conductivity of the binary phases formed during annealing of Ti$_{1-x}$Al$_x$N.

Phases	Thermal Conductivity [W/mK]
c-TiN	20 – 25
c-AlN	5 – 15
w-AlN	12 – 55

3 Experimental Methods

3.1 Coating Deposition

The coatings for this work have been synthesized by reactive unbalanced magnetron sputtering using a lab scale AJA International ATC-1800 UHV sputtering system. Ar was used as working gas and reactive gases were N_2 and O_2. For the plasma etching of the substrates, which was performed before coating deposition, and to apply a negative bias voltage during deposition, an RF power supply was used.

The vacuum chamber of the sputtering system included four water cooled magnetrons, as seen in Figure 3-1, each of them operated by its own power supply. The magnetrons were equipped with one Si target and two Ti/Al targets with 50 at% Ti and 50 at% Al, while the fourth magnetron was blind covered and not in use. The different substrates used were single crystalline silicon strips in 100 orientation with dimensions $7 \times 20 \times 0.38$ mm^3, single crystalline sapphire in 11$\bar{2}$0 orientation with dimensions $10 \times 10 \times 0.5$ mm^3, cemented carbide with 11 wt% Co, 12 wt% mixed carbides and 77 wt% WC in SNUN 120412 geometry (according to ISO 1832), and 0.05 mm thick mild steel foil in form of a disk with a diameter of 12 cm.

The substrates were ultrasonically cleaned in acetone and ethanol each for 5 min and afterwards air dried. Subsequently, three of each type, except the mild steel foil which was coated in a separate deposition run, were mounted on a sample holder fixed on a horizontal rotary device.
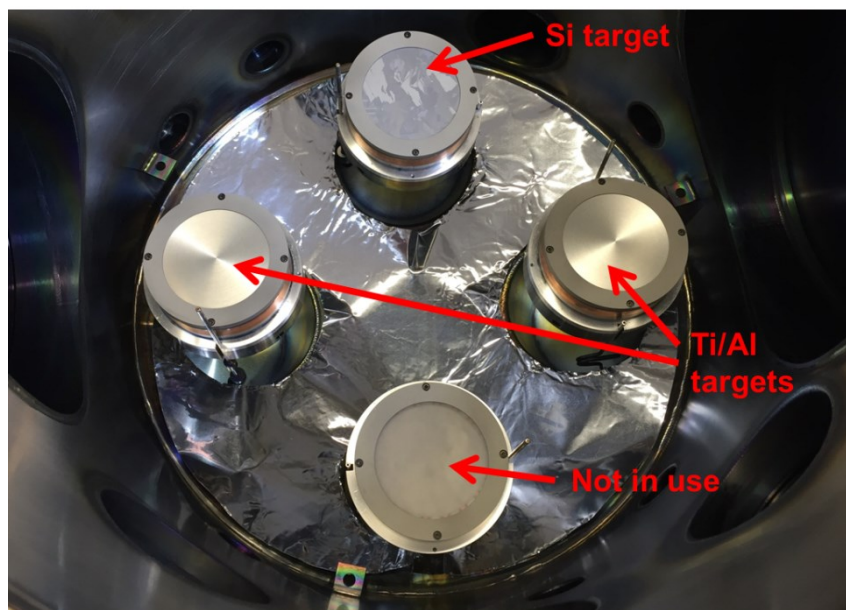

Figure 3-1: Top view of the vacuum chamber used, showing the three magnetrons equipped with Si and Ti/Al targets and the blind covered magnetron not in use.

After evacuation, the substrates were heated to the deposition temperature of 550°C. When a pressure of about 1×10^{-7} mbar was reached, the pressure gauge was set as base pressure and an etching process was performed to remove remaining surface contaminants from the substrates. There, the RF power was set to 40 W for 5 min at a flow rate of 20 sccm for Ar, yielding a pressure of 5×10^{-3} mbar.

After etching the actual deposition was started, as described in detail in sections 3.1.1 and 3.1.2. When the deposition was finished, the heating system was turned off and the substrates were cooled down to 50°C. Then, the pumping system was shut off and the chamber was vented to remove the samples.

3.1.1 Single Layer Coatings

The single layer coatings were grown to perform a basic microstructural investigation on the individual layers and to determine their thermal stability. The SiO_x single layer coatings were deposited on silicon, sapphire and cemented carbide substrates, whereas the $Ti_{1-x}Al_xN$ single layers were grown on silicon, cemented carbide and the mild steel foil. The films on the mild steel foil were used to obtain powder samples for differential scanning calorimetry (DSC, see section 3.2.5), X-ray diffraction (XRD, see section 3.2.4) and for further annealing experiments.

For deposition of both coatings, the total pressure was set to 5×10^{-3} mbar. For synthesis of the SiO_x single layer, the Si target was sputtered in bipolar pulsed DC mode at a power of 400 W, a frequency of 100 kHz and a pause duration of 1 µs at an Ar flow of 20 sccm. The substrates were heated to 550°C and a bias power of 10 W was applied. An oxygen flow of 5 sccm was added to obtain SiO_x films.

For the deposition of $Ti_{1-x}Al_xN$ coatings, the Ti/Al targets were sputtered with a power of 400 W each and a frequency of 2 kHz with a pause duration of 1 µs. The substrate temperature was 550°C and the bias power 20 W. The N_2 flow was set to 7.5 sccm and the flow of Ar to 20 sccm.

The deposition rate was calculated from the resulting coating thickness of the single layer coatings as described in section 3.2.1 and the respective deposition time. The deposition rates of SiO_x and $Ti_{1-x}Al_xN$ were 18 and 19.5 nm/min, respectively. The obtained growth rate allowed to calculate the individual time needed for the deposition of multilayer coatings with adjusted sub-layer thickness.

3.1.2 Multilayer Coatings

The settings used for synthesis of for the sub-layers within the multilayer coatings were the same as for the respective single layers. The duration for the deposition of

the individual layers was adjusted in order to achieve the aimed sub-layer thickness. The total thickness was adjusted to about 20 µm.

Three different multilayer coatings consisting of alternating layers of SiO_x and $Ti_{1-x}Al_xN$ with a thickness ratio of 1:2 were deposited on the silicon and the sapphire substrates. These multilayers were grown to obtain samples with anisotropy in thermal conductivity. The aimed sub-layer and total coating thickness of the multilayer systems are listed in Table 2.

Table 2: Aimed dimensions of the multilayer systems investigated in this thesis.

Nomenclature	Thickness		
	$Ti_{1-x}Al_xN$ layer [nm]	SiO_x layer [nm]	Multilayer [µm]
ML 200/100	200	100	20
ML 100/50	100	50	20
ML 50/25	50	25	20

Under the assumption that the multilayer coatings should have a total thickness of about 20 µm, the deposition time for each multilayer would be nearly 24 hours. Thus, the deposition process was split into two days. For the over-night break the chamber remained closed and evacuated, whereas the heating was switched off.

3.1.3 Powder Production

The $Ti_{1-x}Al_xN$ powder for XRD, DSC and further annealing treatment was produced by dissolving the coated mild steel foil in a heated 20 mol% aqueous dilute nitric acid (HNO_3). This process was done twice to ensure that the whole steel substrate was dissolved, whereas the coating was not affected by the solution. Subsequently, the residual coating was separated from the solution using a filter and washed with distilled water, acetone and ethanol. Finally, it was dried and ground with a mortar to obtain a homogeneous fine grained powder.

3.1.4 Post Treatment

One sample of each multilayer system on sapphire, a sample of the single layer $Ti_{1-x}Al_xN$ on cemented carbide and a part of the $Ti_{1-x}Al_xN$ powder were annealed in a vacuum furnace (HTM Reetz, base pressure < 5×10^{-6} mbar) at 1300°C, using a heating rate of 20 K/min, a holding time of 15 min, and a cooling rate of 60 K/min. The aim of this treatment was to modify the thermal conductivity of the $Ti_{1-x}Al_xN$ sub-layers and, thus, to increase the anisotropy of thermal conductivity of the multilayer coatings. The $Ti_{1-x}Al_xN$ single layer on the cemented carbide substrate served as

reference, whereas the powder sample was used to determine if after annealing decomposition and phase transformation of the $Ti_{1-x}Al_xN$ was completed.

3.2 Coating Characterization

3.2.1 Coating Thickness

Cross-sections of the single layer coated silicon samples were investigated with a scanning electron microscope (SEM) of type Zeiss Auriga SMT to determine the coating thickness. Since SiO_x is electrically isolating, the sample had to be coated with a thin film of gold in order to avoid charging effects. In contrast, $Ti_{1-x}Al_xN$ is electrically conductive and thus this sample could be investigated without gold coating.

The thickness of the multilayers was measured on the silicon substrates using the ball crater technique utilizing a CSM Calowear test. There, a steel ball was first covered with a 1 µm diamond suspension and then rotated on the sample surface. Due to the rotation of the ball, a spherical calotte was ground into the coating, which needed to extend through the coating into the substrate. With a light optical microscope (LOM) of type Reichert Polyvar-Met, the inner and outer diameter of the calotte could be measured. These diameters were subsequently used to calculate the coating thickness [31].

3.2.2 Layer Architecture

Cross-sections of multilayer coated silicon samples were investigated by SEM to receive detailed information about the layer architecture. Micrographs with different magnifications were gathered to determine the actual sub-layer thickness. Cross-sections of the annealed samples were prepared using a focused ion beam (FIB) workstation of type Orsay Physics Cobra Z-05 and also investigated with the SEM to check if the multilayer structure was still intact after the occurred phase transformation.

3.2.3 Chemical Composition

To determine the chemical composition of the $Ti_{1-x}Al_xN$ layers, a cross-section of the single layer sample on silicon was analyzed by means of energy-dispersive X-ray emission spectroscopy (EDS), using an EDAX Apollo 40+ EDS detector providing a resolution of 10 eV, attached to the SEM.

3.2.4 Crystallographic Structure

XRD measurements were performed using a Bruker-AXS D8 Advance diffractometer equipped with Cu Kα radiation, to characterize the crystallographic structure. The tube voltage was set to 40 kV and the tube current to 40 mA. Grazing incidence scans with an incidence angle of 2° and also locked-coupled scans for the coatings grown on mild steel foil were performed. The samples were scanned from 20 to 85° with a step size of 0.02° and a step time of 1.2 seconds per step.

One SiO_x single layer sample grown onto a silicon substrate and for each multilayer, a sample grown onto a sapphire substrate was measured. The coated foil and the gained powder before and after the DSC measurement as well as a powder sample after annealing were also measured.

3.2.5 Thermal Stability

To gain information on the thermal stability of the $Ti_{1-x}Al_xN$ layer, the coating powder was investigated by DSC. There, 14.08 mg of the powder were filled in an aluminum oxide crucible, which was placed together with an empty reference crucible in a Setaram Labsys Evo 1600 DSC. The measurement was performed in Ar atmosphere with a heating rate of 23 K/min starting from room temperature to 1500°C. Two consecutive runs were performed to detect the signal of the metastable sample as well as a baseline signal, which was then subtracted from the first run. The determined DSC signal, a voltage versus temperature curve, allowed identifying the onset and end of spinodal decomposition and subsequent phase transformation as well as interpretation of individual peaks during this sequence.

3.3 Thermal Conductivity

3.3.1 Sample Preparation

The coated sapphire samples were used for the thermal conductivity measurements. There, the surfaces of the samples had to be mirror polished. This is crucial for obtaining a high reflectivity and thus a high intensity of the probe beam reflected from the sample surface. The polishing was performed in two steps using a 3 µm and a 1 µm diamond polishing suspension. Subsequently, one of each multilayer sample was glued on the side of a blank cemented carbide sample using an Agar Scientific Leit-C conductive carbon glue. The cemented carbide samples with a size of $4{\times}6{\times}12$ mm^3 served as sample holder. The cross-sections of the multilayer sample were prepared with a Hitachi IM4000 broad Ar^+ ion-beam polishing system to obtain a smooth and plain surface for the in-plane measurements. Afterwards, the sample for the cross-plane measurement was glued on the top of the cemented carbide

sample holder. To ensure successfully prepared cross-sections with a smooth surface large enough for the TDTR measurements, micrographs of the different multilayers were recorded with LOM.

3.3.2 Measurement

The TDTR measurements were carried out at the Fraunhofer Institute for Physical Measurement Techniques IPM in Freiburg, Germany. This section provides a description of the measurement procedure.

The samples were coated with a 70 nm thick Al layer by electron beam evaporation. For the cross-plane measurements performed on the surface of the samples, a higher thermal penetration depth of the pump beam was needed. This ensured that for the multilayer systems several alternating layers were probed, yielding a representative average thermal conductivity of the system. This was achieved by changing the band-pass filter to a model with a lower modulation frequency of 1.2 MHz instead of the typical 11.1 MHz. The adjusted beam power of the laser was 20 mW. To gain accuracy, four or even five individual measurements on different positions of the sample were performed.

For the in-plane measurements, the beam diameter had to be smaller than the total layer thickness to ensure that the substrate does not affect the measurement. This was accomplished by a focus lens. Because the laser beam of the TDTR holds a Gauss-profile, the diameter of the beam was determined as the $1/e^2$ value of the intensity, i.e. the position where the laser beam dropped to the $1/e^2$ part. The consequently emitted beam diameter was determined to have a size of ~ $14{\times}18$ μm^2. Since positioning of the laser beam was critical for the in-plane measurements, special emphasis was laid on the following steps:

- The beam was moved to the edge of the prepared cross-section until a part of the beam was cut-off and the probe signal was clearly changing.
- Then the beam was carefully moved away from the sample edge towards the substrate until no cut-off could be detected.
- At the same time, the height of the measuring signal was monitored. If this signal was obviously changing, it was taken as a sign that the beam was already in the substrate and it had to be moved back towards the edge.

For the analysis of the thermal conductivity, a model of a semi-infinite solid was used [32]. The in-plane measurement did not correlate completely with this model, because the sample was not rotation-symmetric and on the sample edge the heat flow was cut off. But since the thermal penetration depth was limited in comparison to

the beam diameter, the heat flow could be assumed as one-dimensional. So the heat flow lateral to the surface was confined and therefore this model could be applied.

Since during the measurement, heat is generated by the laser irradiation, the so called steady-state temperature increases. For the individual measurements it stays constant but should be considered while discussing the results obtained. For the measurements performed within this work, the steady-state temperature only differed between the multilayer and the single layer samples, because of the different coating thickness and the different substrates with variable thermal conductivity. The resulting temperature increase for the multilayer was ~40°C and for the single layer ~3°C. Thus, it is important to pay attention to the temperature difference between these two measurements, if they are compared.

4   Results and Discussion

4.1   Single Layer Coatings

Figure 4-1 shows the SEM micrographs of fracture cross-sections of the single layer coatings. These micrographs were used to determine the coating thickness t and to describe the morphology of the coatings. The SiO_x coating appears feature-less as expected for amorphous growth [33], whereas the $Ti_{1-x}Al_xN$ coating is characterized by the unambiguous formation of crystallites.

With the obtained single layer coating thickness and the respective deposition time, the deposition rates were calculated and are listed in Table 3.
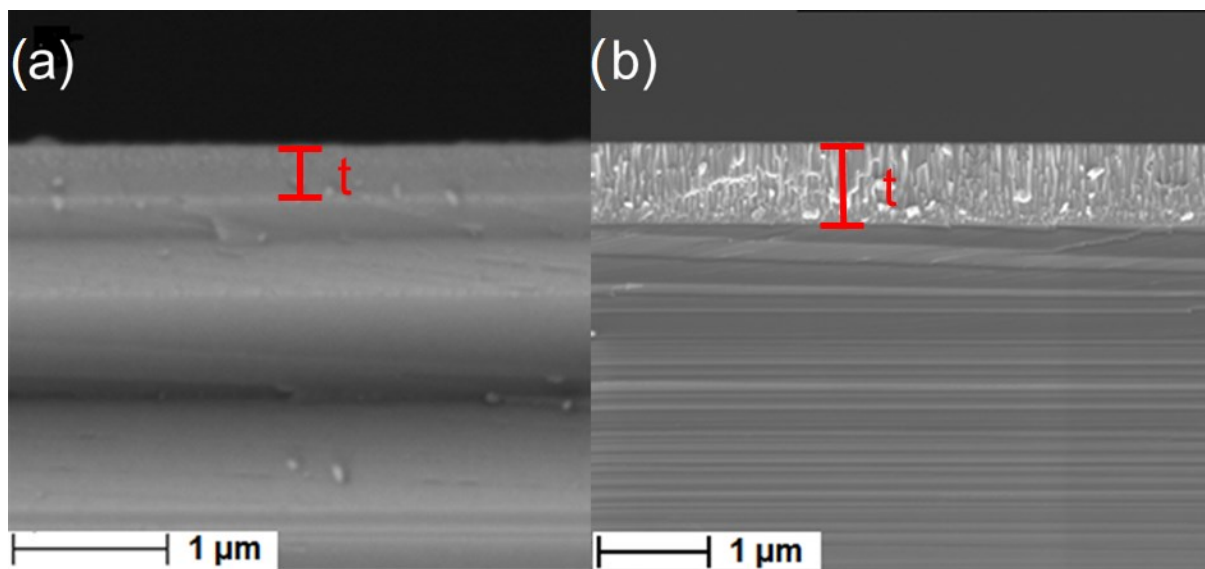

Figure 4-1: SEM micrographs of the single layer coatings investigated within this work. (a) Backscattered electron image of SiO_x and (b) secondary electron image of $Ti_{1-x}Al_xN$. The measured coating thickness t is marked.

Table 3: Thickness, deposition time and calculated deposition rate of the single layer coatings investigated within this thesis.

Coating	Thickness t [nm]	Deposition Time [min]	Deposition Rate [nm/min]
SiO_x	324	18	18
$Ti_{1-x}Al_xN$	779	40	19.4

According to the target composition of 50 at% Ti and 50 at% Al, a $Ti_{1-x}Al_xN$ coating with a metallic proportion of 50/50 was expected to form. However, in fact, the synthesized $Ti_{1-x}Al_xN$ coatings hold a higher Al fraction with a metallic proportion of

40.1/59.9, as determined by EDS. This could be caused by the higher sputtering yield of Al compared to Ti, as already suggested by Kutschej et al. [24].

Figure 4-2 shows the grazing incidence XRD scan of the SiO_x single layer coating. This scan confirms that the SiO_x coating grew amorphous, since only amorphous scattering at low diffraction angle without any diffraction peaks was detected.
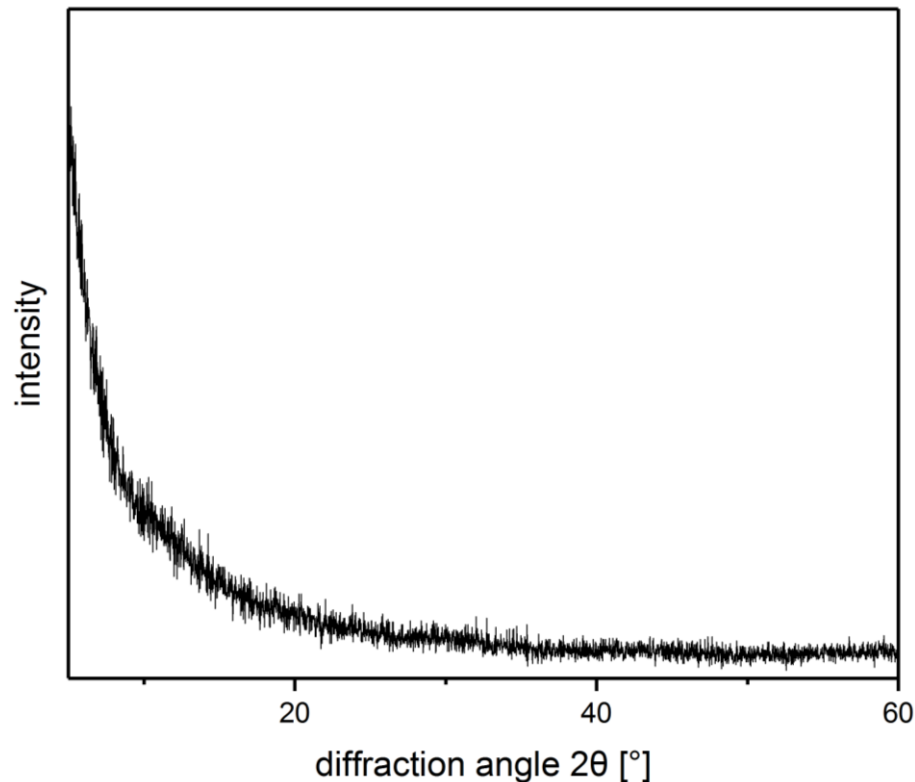

Figure 4-2: Grazing incidence XRD scan of the amorphous SiO_x single layer coating, were only amorphous scattering at low diffraction angle is visible.

In Figure 4-3 the grazing incidence and the locked-coupled XRD scans of the $Ti_{1-x}Al_xN$ coatings grown on the mild steel foil can be seen. These two scans exhibit slight differences, which are however considered as not significant. In addition, the locked-coupled scan of the $Ti_{1-x}Al_xN$ powder is shown Figure 4-4. In both Figures, the detected peaks are located between the standard peak positions of c-TiN and c-AlN, evidencing that a solid solution of $Ti_{1-x}Al_xN$ with a lattice parameter of 4.18 Å (determined using Bragg`s law [17]) was formed. The lattice parameter for c-AlN is 4.12 Å (ICDD 00-025-1495) and for c-TiN 4.24 Å (ICDD 00-038-1420).
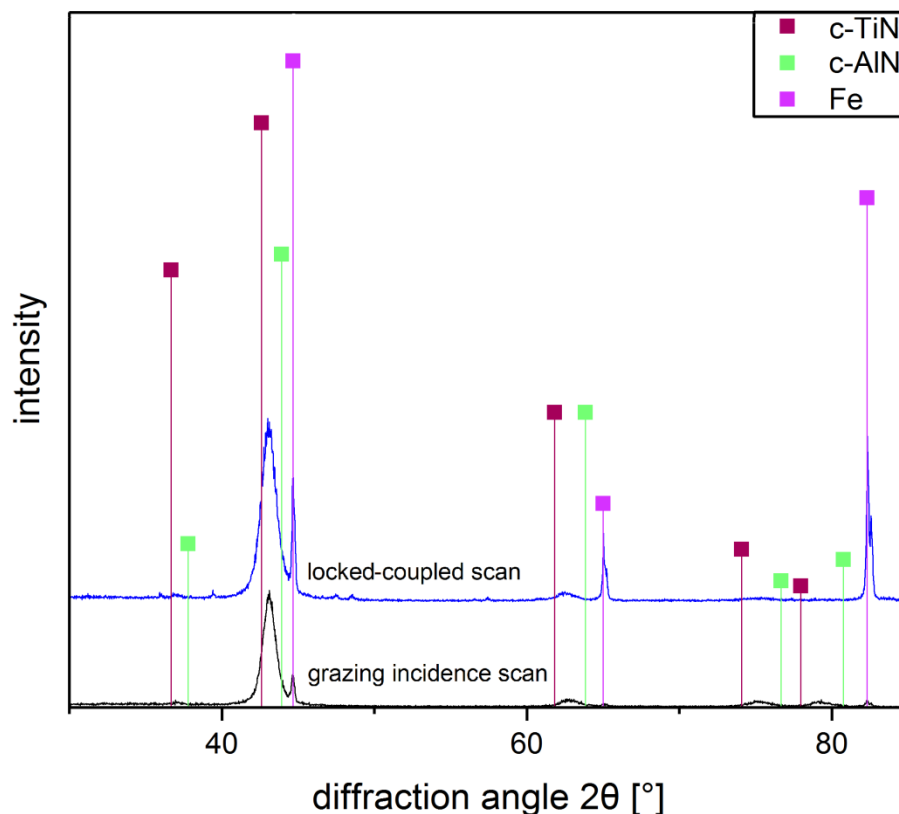
Figure 4-3: XRD scans of the Ti$_{1-x}$Al$_x$N coated mild steel foil in two different diffraction modes with the standard peak positions of c-TiN, c-AlN and Fe indicated. The Fe peaks stem from the mild steel foil used as substrate.
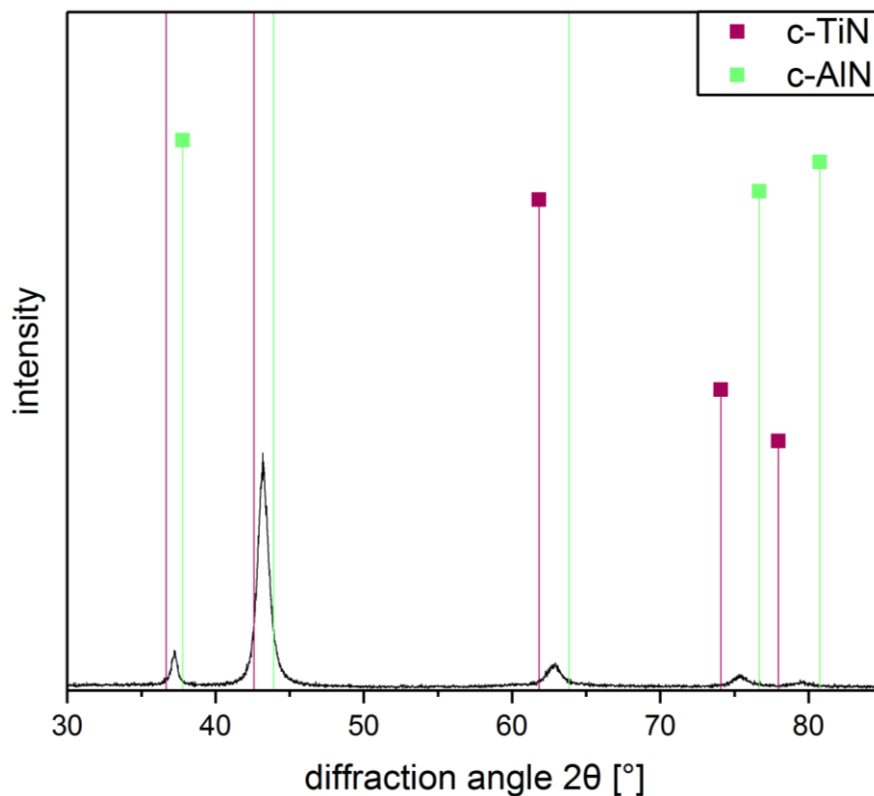

Figure 4-4: Locked-coupled XRD scan of the Ti$_{1-x}$Al$_x$N powder with the standard peak positions of c-TiN and c-AlN indicated.

The measured DSC curve of the $Ti_{1-x}Al_xN$ powder is illustrated in Figure 4-5 and enables to gain information on its thermal stability. The processes occurring are all of exothermic nature. At about 700°C, recovery starts and subsequently spinodal decomposition into c-AlN and c-TiN takes place. At temperatures of about 1000°C, the formed c-AlN transforms into w-AlN. At even higher temperatures of about 1100°C, grain growth occurs. The classification of the fitted peaks corresponds to the findings reported by Mayrhofer et al. [26], where the DSC peaks are located at similar temperatures. At about 1200°C, all decomposition and transformation processes are finished. Consequently, within this thesis a further high vacuum annealing treatment was done at 1300°C, to ensure that the annealed samples are fully decomposed with a transformed microstructure consisting of c-TiN and w-AlN.

The locked-coupled scans of the annealed $Ti_{1-x}Al_xN$ powders, one obtained by thermal ramping in the DSC and the other one annealed in a high vacuum furnace, are shown in Figure 4-6. There, the detected peaks are located at the same position as the standard peaks of c-TiN and w-AlN with lattice parameters a of 4.24 Å (ICDD 00-038-1420) and 3.11 Å (ICDD 00-025-1133). Thus, it can be concluded that both, spinodal decomposition and phase transformation, are indeed finalized for both annealed powders.
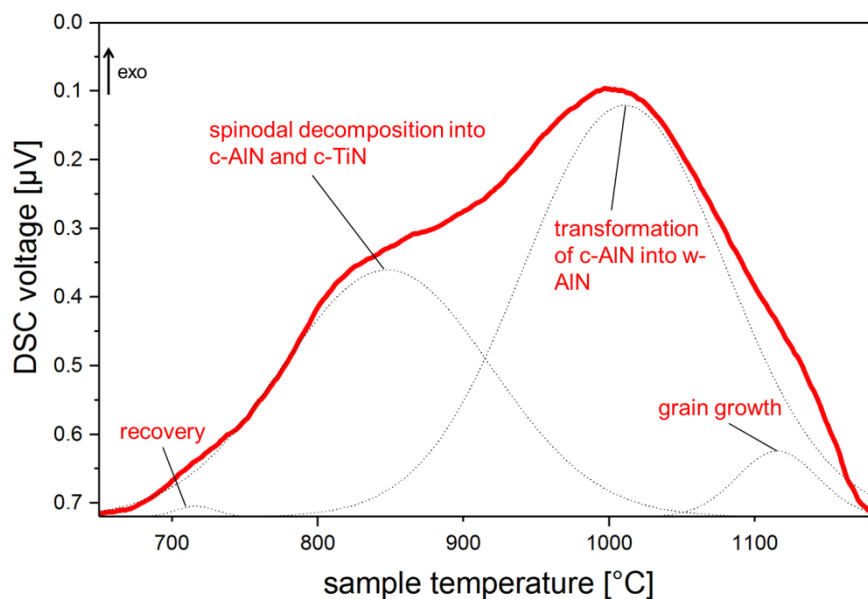

Figure 4-5: DSC curve of $Ti_{1-x}Al_xN$ powder, with the peaks of recovery, spinodal decomposition, phase transformation and grain growth indicated according to ref. [26]. The peaks were fitted using Gaussian functions.
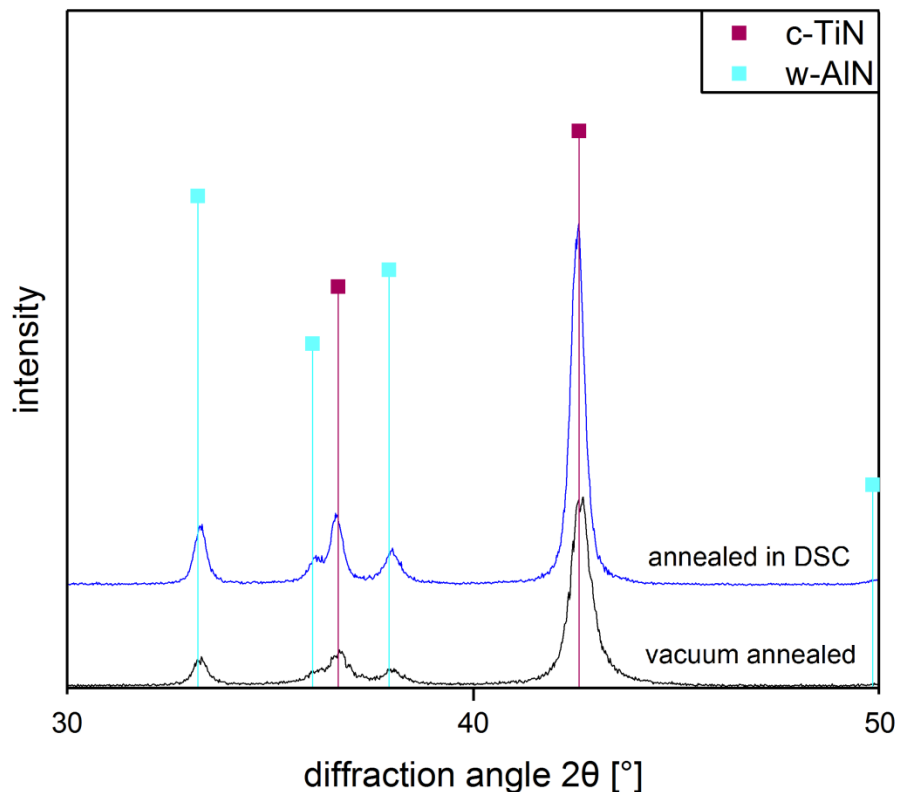
Figure 4-6: Locked-coupled XRD scans of the annealed $Ti_{1-x}Al_xN$ powders, one obtained by thermal ramping in the DSC and the other one annealed in a high vacuum furnace, with the standard peak positions of c-TiN and w-AlN indicated.

4.2 Multilayer Coatings

The predicted deposition rates for the multilayer coatings, which were calculated from the respective single layer coating thicknesses (see Table 3), necessitated a relatively long deposition time of approximately 24 hours for the about 20 µm thick multilayer coatings. Thus, the deposition process was split into two days, with an over-night deposition break, where the samples were kept in the deposition chamber without venting.

The measured coating thicknesses of the different multilayer systems studied within this thesis are listed in Table 4. The aimed total thickness of about 20 µm could be reached for each multilayer.

SEM micrographs, which provide general information on the morphology of the different multilayer systems, are presented in Figure 4-7. In these micrographs the interface, which was formed due to the over-night break during the sputter deposition process because of surface coverage with residual gases present in the vacuum chamber, can clearly be seen.

Table 4: Thickness of the multilayer systems investigated within this thesis.

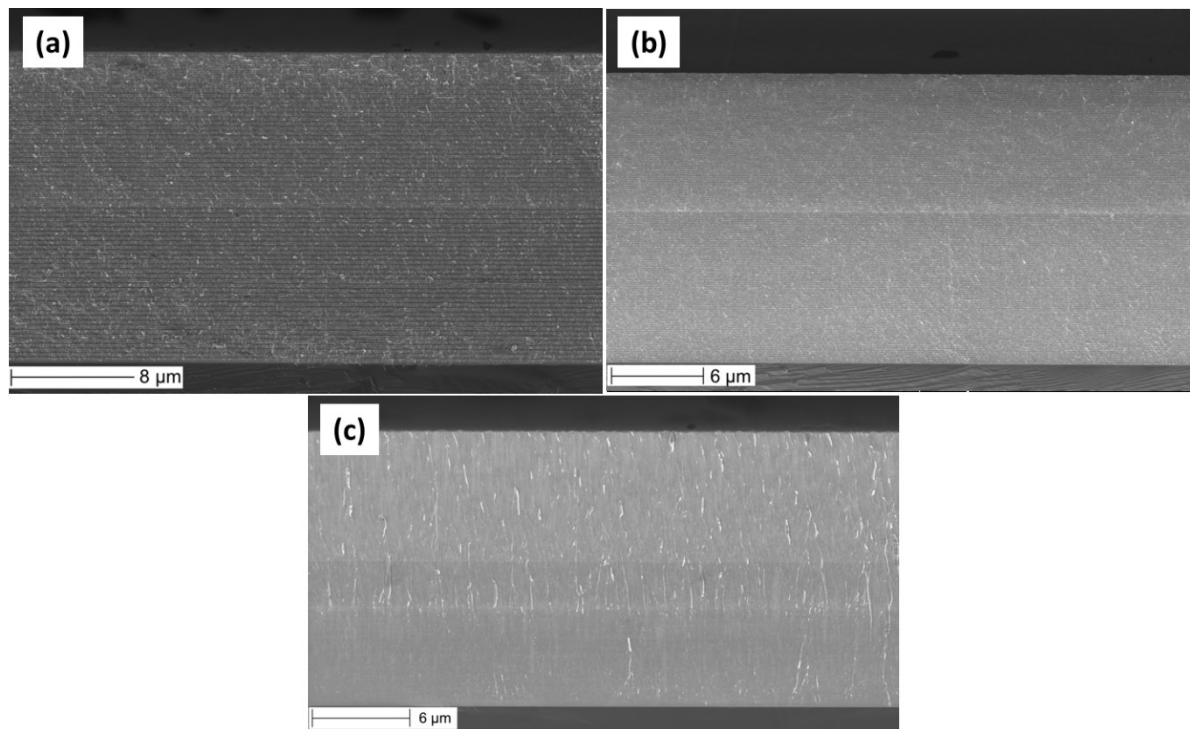| Nomenclature	Thickness [μm]
ML 200/100	20.89
ML 100/50	18.91
ML 50/25	18.76

Figure 4-7: Secondary electron SEM micrographs of the different multilayer systems in the as-deposited state. (a) ML 200/100 (b) ML 100/50 and (c) ML 50/25.

Figure 4-8 represents high magnification SEM micrographs of the multilayer coatings already shown in Figure 4-7. There, the alternating layers of the amorphous SiO_x and the crystalline $Ti_{1-x}Al_xN$ can be clearly distinguished. Figure 4-9 shows an even higher magnification SEM micrograph of the ML 50/25 coating, where a wavelike formation of the sub-layers as a result of nucleation and island growth [12] is visible.

In the high magnification SEM micrographs presented in Figure 4-10, the sub-layer dimensions of the different multilayer systems are added. The obtained thicknesses correspond well to the aimed dimensions of the multilayer systems, as listed in Table 2 in section 3.1.2.
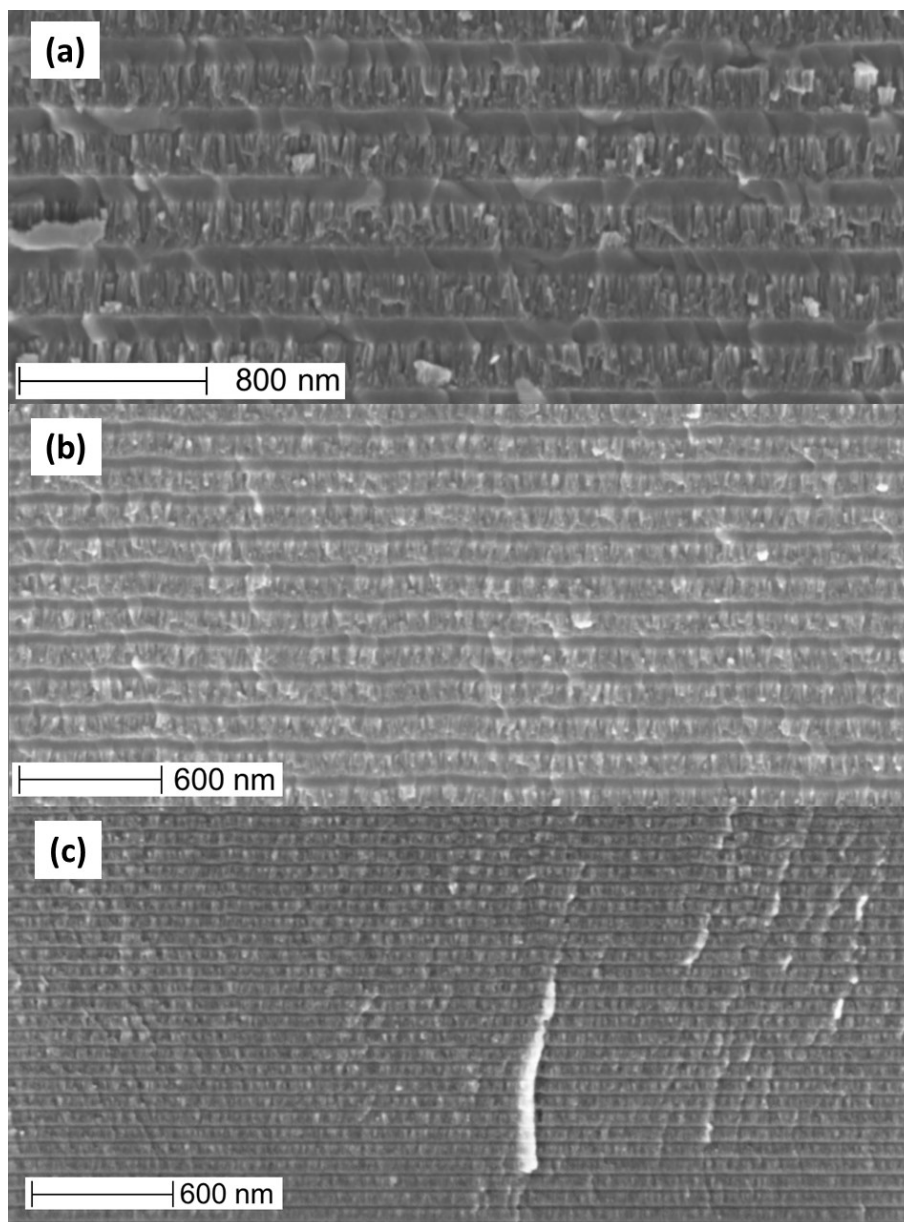
Figure 4-8: High magnification secondary electron SEM micrographs of the different multilayers in the as-deposited state (a) ML 200/100 (b) ML 100/50 and (c) ML 50/25, representing the morphology with the amorphous SiO_x and the crystalline $Ti_{1-x}Al_xN$ sub-layers.
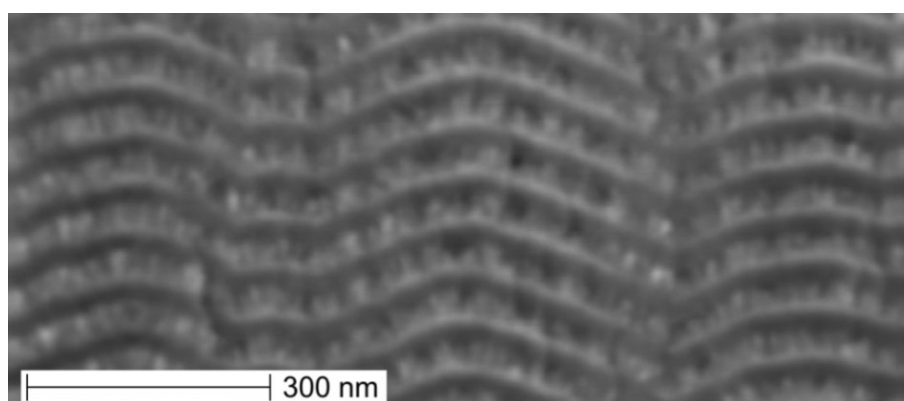

Figure 4-9: Higher magnification secondary electron SEM micrograph of the ML 50/25 sample representing the morphology in the as-deposited state.
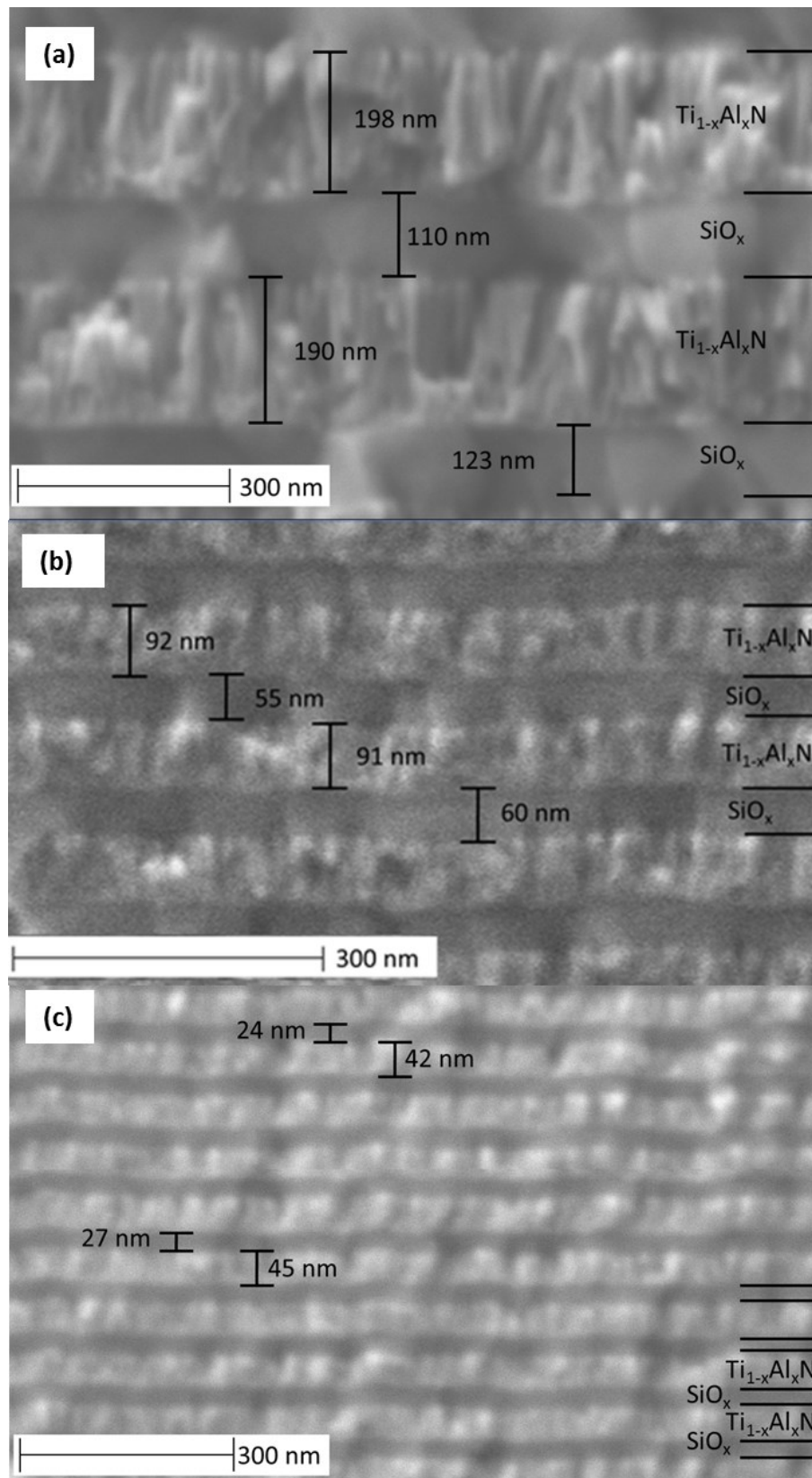
Figure 4-10: Highest magnification backscattered electron SEM micrograph of the amorphous SiO$_x$ and the crystalline Ti$_{1-x}$Al$_x$N sub-layers for the multilayers (a) ML 200/100 (b) ML 100/50 and (c) ML 50/25 in the as-deposited state with the layer dimensions indicated.

The grazing incidence XRD scans of the different multilayer coatings are presented in Figure 4-11. The detected peaks are located between the standard peak positions of c-TiN and c-AlN. This implies that - besides the amorphous SiO_x layer - a $Ti_{1-x}Al_xN$ solid solution was formed. The diffraction peaks broaden with decreasing sub-layer thickness, which indicates grain refinement within the thinner $Ti_{1-x}Al_xN$ sub-layers [34]. The SiO_x phase could not be detected, due to its amorphous nature.
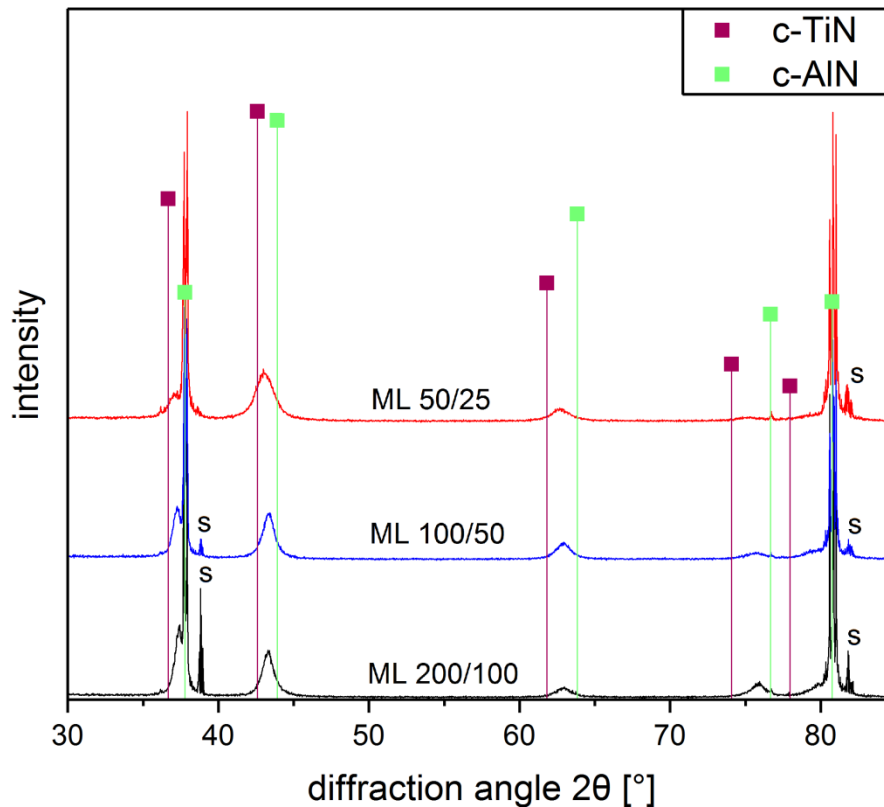

Figure 4-11: Grazing incidence XRD scans of the different multilayers in the as-deposited state with the standard peaks of c-TiN and c-AlN indicated. The peaks labeled with "s" stem from the sapphire substrate.

Figure 4-12 shows the multilayer samples grown on sapphire substrates after the annealing treatment in the high vacuum furnace. The multilayer ML 50/25 was the only one to survive the annealing treatment. This is attributed to its small sub-layer thickness, which may result in low strains due to the low volume of transformed c-AlN phase within the thin sub-layers. Also a Hall-Petch and a thin film effect can be assumed, since the yield stress of coatings increases with decreasing grain size and sub-layer thickness as reported by Arzt et al. [35]. In contrast, the samples with the multilayers ML 200/100 and ML 100/50 were broken and the coatings spalled off the substrate after annealing, probably because of the thicker sub-layer thickness resulting in higher transformation strains and lower yield stresses.
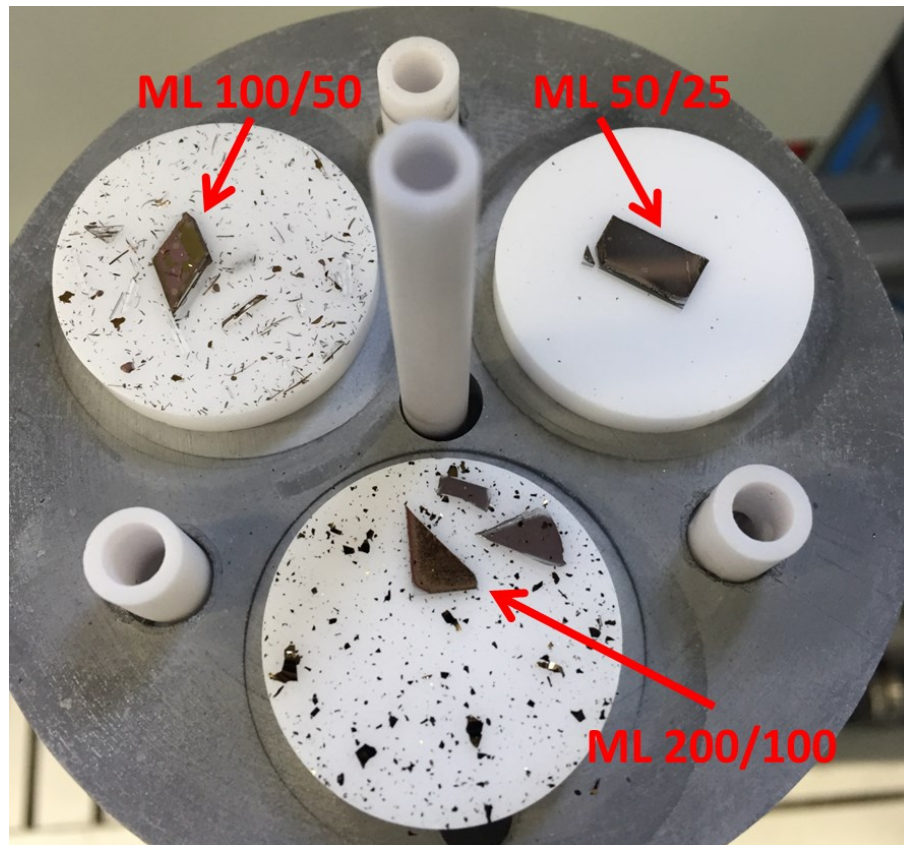
Figure 4-12: View of the sample holder of the vacuum furnace after annealing at 1300°C for 15 min, showing the broken samples and spalled off coating fragments of the multilayers ML 200/100 and ML 100/50 as well as the multilayer ML 50/25, which was the only one to survive annealing.

In Figure 4-13 SEM micrographs of the annealed multilayer ML 50/25 are shown. Figure 4-13 (a) gives an overview of the annealed multilayer, where a difference in porosity in the upper and lower half can be identified. This difference is clearly evident in the higher magnification SEM micrographs of the upper (Figure 4-13 (b)) and the lower half (Figure 4-13 (c)). According to Rachbauer et al. [36], spinodal decomposition of $Ti_{1-x}Al_xN$ into c-TiN and c-AlN is supported by lower grain sizes, leading to more diffusion pathways for Al, which leads according to Hollerweger et al. [37] to the formation of pores.

The SEM micrographs presented in Figure 4-13 (b) and (c) show the morphology of the annealed multilayer ML 50/25. It is evident from Figure 4-13 (b) that the wave like formation of the sub-layers is still intact after annealing.
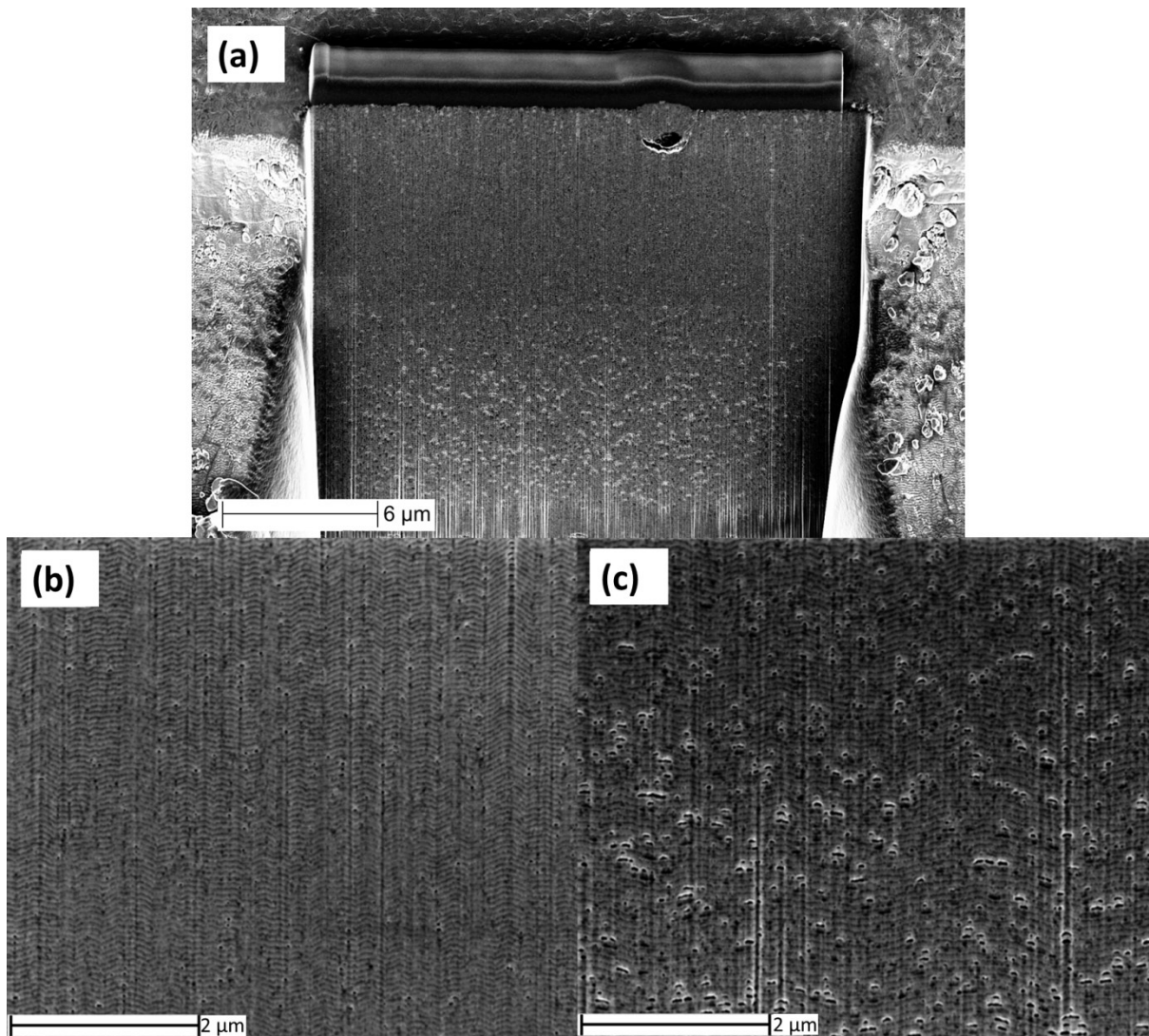
Figure 4-13: Secondary electron SEM micrographs of the annealed multilayer ML 50/25 in different magnifications showing (a) the FIB cut, (b) the morphology of the upper half and (c) the morphology of the lower half of sample ML 50/25, with the different porosity.

In the grazing incidence XRD scan of the annealed multilayer ML 50/25 depicted -in Figure 4-14, the detected peaks are located at the positions of the c-TiN and w-AlN phases. Consequently, it can be concluded that both spinodal decomposition and phase transformation from c-AlN into w-AlN have been completed. Additionally, a new quaternary phase of type $Si_3Al_3O_3N_5$ with a wurtzitic crystal structure and a lattice parameter a of 7.68 Å and c of 2.97 Å (ICDD 01-079-0483) was formed. This phase is characterized by a high hardness, wear resistance, thermal stability and low thermal expansion [38,39].
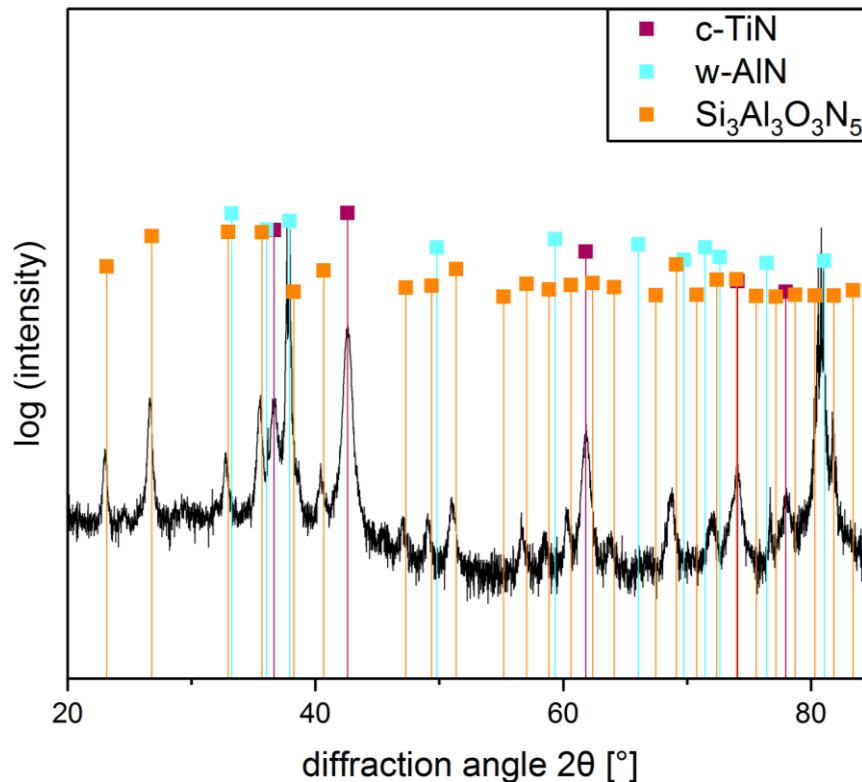
Figure 4-14: Gracing incidence XRD scan of the annealed multilayer ML 50/25 with the standard peaks of c-TiN, w-AlN and Si₃Al₃O₃N₅ indicated.

4.3 Thermal Conductivity

Figure 4-15 shows a cemented carbide sample holder with a multilayer sample glued on for cross-plane and in-plane measurement of the thermal conductivity. The in-plane measurement was performed on the ion-beam polished surface of coating cross-sections of the multilayer sample glued onto the side of the cemented carbide sample holder.

Figure 4-15: Cemented carbide sample holder with the multilayer ML 200/100 samples glued on for the in-plane and cross-plane measurements of thermal conductivity.

A representative LOM micrograph of the ion-beam polished cross-sectional surface of the multilayers is presented in Figure 4-16. All prepared surfaces were smooth and large enough for the measurement with the ~ 14×18 µm^2 laser beam.
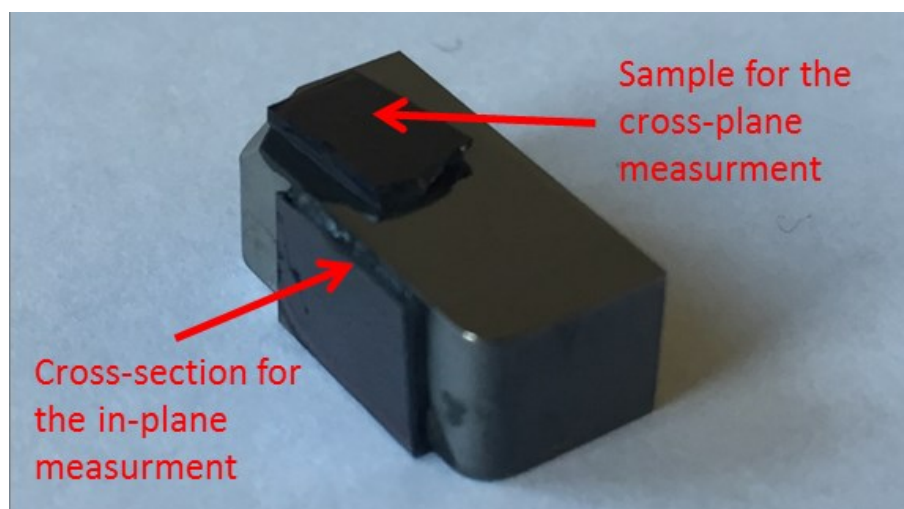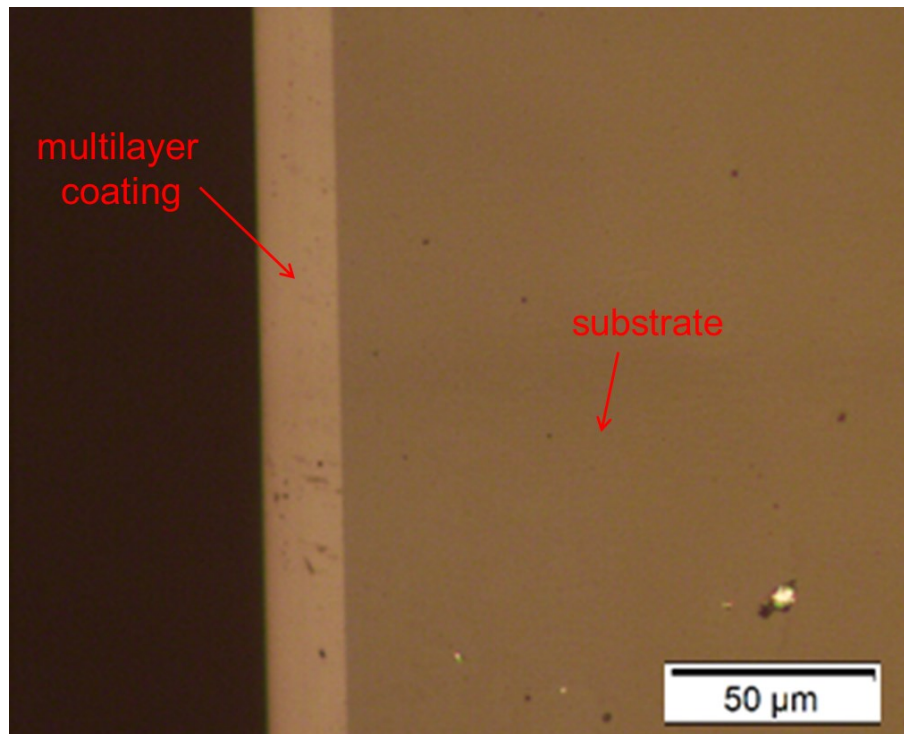

Figure 4-16: Representative LOM micrograph of the ion-beam polished cross-section of the multilayer ML 200/100.

In Table 5 the results determined by the TDTR measurement and the calculated specific heat capacity c_p as well as the anisotropy in the thermal conductivity F are listed. There, the specific heat capacity c_p of the different coatings is based on literature values of SiO$_x$ [40], TiN and AlN [41–43]. The values of TiN and AlN were used to calculate the specific heat capacity of Ti$_{1-x}$Al$_x$N applying the Neumann-Koppsche rule [44]. The latter implies that the molecular heat of a polyatomic solid body is equivalent to the sum of the molecular heats of the individual components. In Table 5, $\kappa_\perp$ represents the cross-plane and $\kappa_\parallel$ the in-plane thermal conductivity. The estimated variance of the respective thermal conductivity is given by Δ. The anisotropy in the thermal conductivity F was also calculated using equation (2) in section 2.2.3.

Table 5: Overview of the specific heat capacity c_p, the determined cross-plane $\kappa_\perp$ and in-plane $\kappa_\parallel$ thermal conductivity with their estimated variance Δ and the resulting anisotropy factor F of the single layer and the different multilayer coatings.

Nomenclature	c_p [J/cm³K]	$\kappa_\perp$ [W/mK]	Δ [W/mK]	$\kappa_\parallel$ [W/mK]	Δ [W/mK]	F [ ]
SiO$_x$ as-deposited	1.62	**1.6**	0.2	-	-	-
Ti$_{1-x}$Al$_x$N as-deposited	2.69	**3.8**	0.6	-	-	-
Ti$_{1-x}$Al$_x$N annealed	2.69	**24.0**	4.0	-	-	-
ML 200/100	2.29	**2.8**	0.4	**3.2**	0.5	1.14
ML 100/50	2.27	**3.1**	0.5	**3.0**	0.5	0.97
ML 50/25	2.29	**2.4**	0.5	**2.5**	0.4	1.04
ML 50/25 annealed	2.29	**3.0**	0.5	**3.9**	0.6	1.30

The thermal conductivity value of as-deposited Ti$_{1-x}$Al$_x$N and SiO$_x$, as reported in literature, is around 3.8 W/mK [3] and 1.8 W/mK [19], respectively, which matches well with the determined values of the as-deposited single layers investigated within this thesis. The thermal conductivity of the annealed Ti$_{1-x}$Al$_x$N, reported by Rachbauer et al. [3], increase by a factor of three after annealing. There, the treatment was performed with a holding time of only 1 min, hence, it is possible that the phase transformation of c-AlN into w-AlN was not finalized and therefore the thermal conductivity is lower than the determined value of this work.

The determined in-plane as well as the cross-plane thermal conductivity of the as-deposited multilayers approximately match with the calculated thermal conductivity of 3.05 W/mK, which was estimated by applying a rule of mixture, using the determined values of the single layer Ti$_{1-x}$Al$_x$N and SiO$_x$ coatings and their volume fraction. For the direct comparison of the data obtained for the single layers with those of the multilayers, it should be noted that the substrates used for deposition of single and multilayers were different. This and the unequal layer thicknesses result in a difference of the steady-state temperature increase, as already mentioned in section 3.3.2. The in- and cross-plane thermal conductivities of the different as-deposited multilayers did not differ as much. This means that the different layer architecture of the samples did not significantly affect the thermal conductivity.

The expected anisotropy in thermal conductivity was calculated with equation (1) in section 2.2.2 using the literature values of the thermal conductivity of the formed phases, i.e. 3.8 W/mK for as-deposited Ti$_{1-x}$Al$_x$N [3], 11.4 W/mK for annealed Ti$_{1-x}$Al$_x$N [3] and 1.8 W/mK for SiO$_x$ [19]. The thus calculated anisotropy of all as-deposited and annealed multilayers was 1.13 and 2, respectively. The calculated anisotropy only depends on the ratio of the thicknesses and the thermal

conductivities of the sub-layers. The anisotropy calculated for the different multilayers in the as-deposited state using the experimentally determined values given in Table 5 matches well with the calculated values, if the estimated variance is taken into account. The anisotropy only really differs for the annealed multilayer, because the measured in-plane thermal conductivity was lower than calculated.

Since the thermal conductivity of the $Ti_{1-x}Al_xN$ single layer is increasing significantly after annealing, also a pronounced increase of the in-plane thermal conductivity of the annealed multilayer coating was expected. However, this was not the case and instead, the in-plane thermal conductivity nearly stayed the same as before annealing. There are several reasons which could explain this behavior. One of these reasons could be the formed quaternary phase of type $w\text{-}Si_3Al_3O_3N_5$, as evidenced by XRD (see Figure 4-14). As a bulk material, this phase is characterized by a thermal conductivity of 18 W/mK [45]. This value is possibly lower for thin films due to increasing contributions of grain boundary scattering and phonon leakage in thin film materials [30]. In addition, due to the new phase more grain boundaries are formed, where more phonons are scattered, which in turn again decreases the thermal conductivity. Therefore, the additional $Si_3Al_3O_3N_5$ phase is assumed to reduce the average thermal conductivity of the whole multilayer coating, even if the thermal conductivity of the transformed $Ti_{1-x}Al_xN$ phase increases significantly (see Table 5). Another reason for the low thermal conductivity, even after annealing, could be the prevented grain growth caused by the SiO_x layers, which surround the $Ti_{1-x}Al_xN$ layers, which was established by Vepřek et al. [46] for the TiN/SiN system.

5 Summary and Conclusion

The aim of this work was to develop a possibility to measure not only the cross-plane but also the in-plane thermal conductivity of hard coatings using TDTR. Reaching this goal, the anisotropy of thermal conductivity whithin multilayer systems, as e.g. used to protect cutting tools against wear, should become measurable. To achieve this, a special ion-beam assisted preparation procedure for coating cross-sections and subsequent in-plane TDTR measurements was developed and applied to different multilayer systems. Further, possible changes in anisotropy of the thermal conductivity for selected multilayers after annealing were investigated.

At first, single layer coatings of amorphous SiO_x and crystalline $Ti_{1-x}Al_xN$ were synthesized by reactive magnetron sputter deposition to determine their microstructure, elemental composition, thermal stability and thermal conductivity in the as-deposited state. Subsequently, multilayer systems consisting of alternating layers of these two materials with different sub-layer thicknesses were deposited to investigate anisotropy effects. Selected multilayer samples were vacuum annealed to explore whether the anisotropy in thermal conductivity can be influenced.

TDTR measurements indicated that the as-deposited multilayers only showed a minor anisotropy. After annealing at 1300°C, the expected and also calculated anisotropy using the single layer thermal conductivities was not obtained for the multilayer. This could be explained by the appearance of an additional $w-Si_3Al_3O_3N_5$ phase formed by interface reactions between SiO_x and $Ti_{1-x}Al_xN$ and by the prevention of grain growth, caused by the periodicity of interfaces between the individual layers.

Nevertheless, in conclusion, a new method for in-plane thermal conductivity measurements using TDTR was developed and successfully tested on several multilayer coatings. For the future, this method offers a new playground for the design and subsequent characterization of coatings with anisotropic thermal conductivity. However, validation of the results obtained for thin films by using reference samples of thick coatings with well-defined in- and cross-plane thermal conductivities would is highly recommended.

6 References

[1]   P.H.M. Böttger, A. V. Gusarov, V. Shklover, J. Patscheider, M. Sobiech, Anisotropic layered media with microinclusions: Thermal properties of arc-evaporation multilayer metal nitrides, Int. J. Therm. Sci. 77 (2014) 75–83.

[2]   L. Braginsky, A. Gusarov, V. Shklover, Models of thermal conductivity of multilayer wear resistant coatings, Surf. Coat. Technol. 204 (2009) 629–634.

[3]   R. Rachbauer, J.J. Gengler, A.A. Voevodin, K. Resch, P.H. Mayrhofer, Temperature driven evolution of thermal, electrical, and optical properties of Ti-Al-N coatings, Acta Mater. 60 (2012) 2091–2096.

[4]   P.H.M. Böttger, L. Braginsky, V. Shklover, E. Lewin, J. Patscheider, D.G. Cahill, M. Soebich, Hard wear-resistant coatings with anisotropic thermal conductivity for high thermal load applications, J. Appl. Phys. 116 (2014) 1–8.

[5]   M. Sobiech, M.P.H. Böttger, V. Shklover, J. Patscheider, Hard material layers with selected thermal conductivity, Patent WO 2014/154356 A1, 2014.

[6]   C. Mitterer, PVD and CVD hard coatings, in Comprehensive Hard Materials (V.K Sarin (Editor-in-Chief), L. Llanes, D. Mari (Vol.Eds.)). Vol. 2, Elsevier, Amsterdam, 2014, 449–467.

[7]   J.E. Mahan, Physical Vapor Deposition of Thin Films, A Wiley-Interscience Publication, Weinheim, 2000.

[8]   D.M. Mattox, Handbook of Physical Vapor Deposition (PVD) Processing, Noyes Publications, Westwood, 1998.

[9]   R.M. Prengel, H. G., Jindal, P. C., Wendt, K. H., Santhanam, A. T., Hegde, P. L., Penich, A new class of high performance PVD coating for carbide cutting tools, Surf. Coat. Technol. 139 (2001) 25–34.

[10]   C.-T. Huang, J.-G. Duh, Deposition of (Ti,Al)N films on A2 tool steel by reactive r.f. magnetron sputtering, Surf. Coat. Technol. 71 (1995) 259–266.

[11]   M. Ohring, Materials Science of Thin Films, Academic Press, San Diego, 2002.

[12]   P.M. Martin, Handbook of Deposition Technologies for Films and Coatings, Elsevier, Oxford, 2005.

[13]   F. Rovere, Theoretical and experimental assessment of Cr-Al-Y-N as protective coating for y-TiAl based alloys, PhD thesis, Rheinisch-Westfälische Technische Hochschule, 2009.

[14]   S. Paldey, S.C. Deevi, Single layer and multilayer wear resistant coatings of (Ti ,Al)N: a review, Mater. Sci. Eng. 342 (2003) 58–79.

[15]   R. Nave, Thermal Conductivity, http://hyperphysics.phy-astr.gsu.edu/hbase/thermo/thercond.html (accessed December 1, 2016).

[16]   G. Gottstein, Physikalische Grundlagen der Metallkunde, Springer, Aachen, 2007.

[17]   R.E. Hummel, Electronic Properties of Materials, Springer, New York, 2001.

References

[18]   P.H.M. Böttger, E. Lewin, J. Patscheider, V. Shklover, D.G. Cahill, R. Ghisleni, M. Sobiech, Thermal conductivity of hard oxynitride coatings, Thin Solid Films. 549 (2013) 232–238.

[19]   M. Winkler, Time-domain thermoreflectance (TDTR), Diploma thesis, Eberhard-Karls-Universität Tübingen, 2008.

[20]   Y.X. Xu, L. Chen, F. Pei, Y. Du, Structure and thermal properties of TiAlN/CrN multilayered coatings with various modulation ratios, Surf. Coat. Technol. 304 (2016) 512–518.

[21]   A. Hörling, L. Hultman, M. Odén, J. Sojölén, L. Karlsson, Thermal stability of arc evaporated high aluminium-content $Ti_{1-x}Al_xN$ thin films, J. Vac. Sci. Technol. A 20 (2002) 1815–1823.

[22]   V. Moraes, H. Riedl, R. Rachbauer, S. Kolozsvári, M. Ikeda, L. Prochaska, S. Paschen, P.H. Mayrhofer, Thermal conductivity and mechanical properties of AlN-based thin films, J. Appl. Phys. 119 (2016) 1–10.

[23]   A. Kimura, H. Hasegawa, K. Yamada, T. Suzuki, Effects of Al content on hardness, lattice parameter and microstructure of $Ti_{1-x}Al_xN$ films, Surf. Coat. Technol. 121 (1999) 438–441.

[24]   K. Kutschej, P.H. Mayrhofer, M. Kathrein, P. Polcik, R. Tessadri, C. Mitterer, Structure, mechanical and tribological properties of sputtered $Ti_{1-x}Al_xN$ coatings with 0.5≤x≤0.75, Surf. Coat. Technol. 200 (2005) 2358–2365.

[25]   P.H. Mayrhofer, R. Rachbauer, D. Holec, F. Rovere, J.M. Schneider, Protective transition metal nitride coatings, in Comprehensive Hard Materials (V.K. Sarin (Editor-in-Chief), L. Llanes, D. Mari (Vol.Eds.)). Vol. 4, Elsevier, Amsterdam, 2014 355–388.

[26]   P.H. Mayrhofer, A. Hörling, L. Karlsson, J. Sjölén, T. Larsson, C. Mitterer, L. Hultman, Self-organized nanostructures in the Ti-Al-N system, Appl. Phys. Lett. 83 (2003) 2049–2051.

[27]   A. Hörling, L. Hultman, M. Odén, J. Sjölén, L. Karlsson, Mechanical properties and machining performance of $Ti_{1-x}Al_xN$-coated cutting tools, Surf. Coat. Technol. 191 (2005) 384–392.

[28]   M. Kawate, A. Kimura, T. Suzuki, Microhardness and lattice parameter of $Cr_{1-x}Al_xN$ film, J. Vac. Sci. Technol. A20(2) (2002) 569–571.

[29]   S. Hayashi, T. Hirai, Thermal conductivity of chemically vapour-deposited Si_3N_4-TiN composites, J. Mater. Sci. 18 (1983) 3259–3264.

[30]   M. Bogner, G. Benstetter, Y. Qing, Cross- and in-plane thermal conductivity of AlN thin films measured using differential 3-omega method, Surf. Coat. Technol. (2017) 1–6.

[31]   G. Kienel, Vakuumbeschichtung 3, Anlagenautomatisierung – Meß- und Analysentechnik, VDI Verlag, Düsseldorf, Düsseldorf, 1994.

[32]   D.G. Cahill, Analysis of heat flow in layered structures for time-domain thermoreflectance, Rev. Sci. Instrum. 75 (2004) 5119–5122.

References

[33] M.A. Curiel, N. Nedev, D. Nesheva, J. Soares, R. Haasch, M. Sardela, B. Valdez, B. Sankaran, E. Manolov, I. Bineva, I. Petrov, Microstructural characterization of thin SiOx films obtained by physical vapor deposition, Mater. Sci. Eng. B. 174 (2010) 132–136.

[34] M. Birkholz, Thin Film Analysis by X-Ray Scattering, Wiley-VCH Verlag, Weinheim, 2006.

[35] E. Arzt, Size effects in materials dur to microstructural and dimensional constraints: A comparative review, Acta Metall. 46 (1998) 5611–5626.

[36] R. Rachbauer, S. Massl, E. Stergar, D. Holec, D. Kiener, J. Keckes, J. Patscheider, M. Stiefel, H. Leitner, P.H. Mayrhofer, N. However, Decomposition pathways in age hardening of Ti-Al-N films, J. Appl. Phys. 110 (2011) 1–10.

[37] R. Hollerweger, H. Riedl, J. Paulitsch, M. Arndt, R. Rachbauer, P. Polcik, S. Primig, P.H. Mayrhofer, Origin of high temperature oxidation resistance of Ti–Al–Ta–N coatings, Surf. Coat. Technol. 257 (2014) 78–86.

[38] M. Riva, Entwicklung und Charakterisierung von Sialon-Keramiken und Sialon-SiC-Verbunden für den Einsatz in tribologisch hochbeachspruchten Gleitsystemen, Scientific Publishing, Karlsruhe, 2010.

[39] S. Özcan, G. Aç, N. Özbay, N. Çal, The effect of silicon nitride powder characteristics on SiAlON microstructures, densification and phase assemblage, Ceram. Int. 43 (2017) 10057–10065.

[40] D.G. Cahill, Analysis of heat flow in layered structures for time-domain thermoreflectance, Rev. Sci. Instrum. 75 (2004) 5119–5122.

[41] H.O. Pierson, Handbook of Refractory Carbides and Nitrides, William Andrew, Norwich, 1996.

[42] M.W. Chase, Aluminium Nitride, http://webbook.nist.gov/cgi/inchi?ID=C24304005&Mask=2#Thermo-Condensed (accessed June 1, 2017).

[43] M.W. Chase, Titanium Nitride, http://webbook.nist.gov/cgi/inchi?ID=C25583204&Type=JANAFS&Table=on#JANAFS (accessed June 1, 2017).

[44] P. Wagner, G. Reischl, G. Steiner, Einführung in die Physik, Facultas, Wien, 2014.

[45] U. Clemens, Einsatz der CMB-Technologie zur Herstellung von Hinterschneidungen bei metallischen Bauteilen, PhD thesis, Rheinisch-Westfälische Technische Hochschule Aachen, 2004.

[46] V.I. Ivashchenko, S. Veprek, First-principles molecular dynamics study of the thermal stability of the BN, AlN, SiC and SiN interfacial layers in TiN-based heterostructures: Comparison with experiments, Thin Solid Films. 545 (2013) 391–400.